DESIGN OF MINIATURIZED TIME-OF-FLIGHT REFLECTRON MASS SPECTROMETER FOR UPPER ATMOSPHERE DENSITY MEASUREMENTS

by

Michelle Lynn Pyle

A thesis submitted in partial fulfillment
of the requirements for the degree

of

MASTER OF SCIENCE

in

Electrical Engineering

Approved:

Dr. Ryan Davidson Major Professor	Dr. Charles Swenson Committee Member
Dr. Erik Syrstad Committee Member	Dr. Jacob Gunther Committee Member

Dr. Mark R. McLellan
Vice President for Research and
Dean of the School of Graduate Studies

UTAH STATE UNIVERSITY
Logan, Utah

2016

Abstract

Design of Miniaturized Time-of-Flight Reflectron Mass Spectrometer for Upper Atmosphere Density Measurements

by

Michelle Lynn Pyle, Master of Science

Utah State University, 2016

Major Professor: Dr. Ryan Davidson
Department: Electrical and Computer Engineering

Variations of gas and plasma density and composition in Earth's thermosphere and ionosphere are key indicators of interactions between different layers of Earth's atmosphere. The nature of interactions between neutral and ion species in the upper atmosphere is an active area of study in Heliophysics and there is much to learn about the dynamic relationship between the ionosphere and neutral thermosphere. Mass Spectrometers are among an array of instruments used to explore Earth's upper atmosphere and other space environments. In the past, data from mass spectrometers flown in low earth orbit has been used to improve atmospheric models and to study the dynamics of the ionosphere and thermosphere. Historically, these instruments are substantial in size and deployed on larger satellite platforms. Data from these larger instruments generally provide information from a specific point in time at a single location. Studies of atmospheric density and composition with multiple locations for each time point could be performed by CubeSat swarms if proper instrumentation were available to fit CubeSat payload restrictions. The proposed miniaturized time-of-flight (TOF) mass spectrometer (MS) will have a mass resolution and range sufficient for measuring the composition of Earth's thermosphere and ionosphere while operating within the power and space constraints of a CubeSat. The capabilities of this

instrument could dramatically reduce the cost of future missions while simultaneously enhancing the science return. The design employs miniaturization of TOF-MS technology, including resolution refinement techniques used for larger instruments and standard concepts for TOF-MS components such as acceleration grids, a Bradbury-Nielsen wire gate, a gridless ion mirror, and microchannel plate detector.

(97 pages)

Public Abstract

Design of Miniaturized Time-of-Flight Reflectron Mass Spectrometer for Upper Atmosphere Density Measurements

by

Michelle Lynn Pyle, Master of Science

Utah State University, 2016

Major Professor: Dr. Ryan Davidson
Department: Electrical and Computer Engineering

Upper atmosphere and solar events can have strong impacts on the communication, power, and navigation systems we use every day. Modeling atmospheric dynamics, or the changes and reactions of different regions of the atmosphere, can help improve understanding and predictions of the effects of solar events. A suite of measurements of the upper atmosphere, including wind, temperature, and composition measurements, is used to build atmospheric models. Current atmospheric models are very sophisticated but need additional data to fully model atmospheric dynamics. In the past, measurements used to determine atmospheric composition have been performed using mass spectrometer instruments on full-size satellites. Traditional satellites are substantial in size and can be expensive to build and launch. Mass spectrometer measurements taken from a much smaller satellite could be flown closer together and would be less expensive to build and launch. This miniature mass spectrometer project aims to design technology that would enable high-quality mass spectrometer measurements to be taken from a small satellite. The project downsizes some published techniques to improve measurement quality and develops some new technologies for mass spectrometers.

Acknowledgments

This project is supported through funding and expertise by a grant from the National Science Foundation (NSF) Experimental Program to Stimulate Competitive Research (EPSCoR), the Utah State University Research Foundation's Space Dynamics Lab (SDL), a student fellowship award from the Utah NASA Space Grant Consortium (UNSGC), the Utah State University Student Association Research and Projects Grant, and the Center for Space Engineering (CSE) at Utah State University (USU).

Michelle Lynn Pyle

Contents

List of Tables

List of Figures

Acronyms

ADC	Analog to Digital Converter
AIAA	American Institute of Aeronautics and Astronautics
AMU	Atomic Mass Units
APD	Avalanche Photodiode
BNG	Bradbury-Neilsen Gate
CEDAR	Coupling, Energetics, and Dynamics of Atmospheric Regions
CFD	Constant Fraction Discriminator
CPS	Counts Per Second
CSE	Center for Space Engineering
DC	Direct Current
EOM	Equation of Motion
EPSCoR	Experimental Program to Stimulate Competitive Research
FIFO	First In, First Out
FPGA	Field Programmable Gate Array
FTET	Flight Time Estimation Tool
FWHM	Full Width Half Maximum
GSFC	Goddard Spaceflight Center
HDL	Hardware Description Language
LEO	Low Earth Orbit
LVPECL	Low Voltage Positive Emitter Coupled Logic
MCP	Microchannel Plate
MDET	Measurable Density Estimation Tool
MS	Mass Spectrometer
MTOF-MS	Miniature Time-of-Flight Mass Spectrometer
NRLMSISE-00	US Naval Research Lab Mass Spectrometer and Incoherent Scatter Radar Model

NSF	National Science Foundation
PCB	Printed Circuit Board
SDL	Space Dynamics Lab
SNR	Signal-to-Noise Ratio
TOB	Time-of-Birth
TOF	Time-of-Flight
U	Units (10 cm x 10 cm x 10 cm)
UNSGC	Utah NASA Space Grant Consortium
USU	Utah State University

Chapter 1

Design Overview

This is an endeavor to build a CubeSat instrument to measure the composition and density of Earth's upper atmosphere. The research includes the design, fabrication, and testing of components for a miniature time-of-flight mass spectrometry (MTOF-MS) instrument.

1.1 Requirements

The project requirements and design have been chosen to advance space technology by allowing the instrument to make accurate measurements with higher spatial resolution than is currently achieved. Primary requirements for the MTOF-MS are listed in Table 1.1. Most of these requirements are based on a low earth orbit (LEO) mission to demonstrate the instrument's capabilities.

The volume and instrument mass requirements flow down directly from CubeSat acceptance requirements; the instrument will be one of many subsystems on the spacecraft with a maximum mass of 1.33 kg per 1 unit (U, defined as 10 cm^3). The power requirement is a goal meant to make the instrument compatible with the power system on a typical CubeSat bus (about 1 W per 1 U). The mass measurement range, mass resolution, and sensitivity requirements are common metrics for evaluating mass spectrometers and will ensure that the MTOF-MS provides quality measurements. The mass range is designed to allow measurement of all of the molecular and atomic species typically found in the thermosphere and ionosphere along with some metallic ions. The mass resolution is a ratio of the average measured mass of a particle species to the full-width-half-maximum (FWHM) of the distribution curve of the mass measurements for that constituent (see Equation 1.1). The spatial resolution requirement states how closely-spaced the along-track measurements should be. This requirement surpasses the spatial resolution required to measure the thermosphere.

Table 1.1: Instrument Requirements

Primary Instrument Requirements	
Instrument Volume	1/2 U (10 cm x 10 cm x 5 cm)
Electronics Volume	1/2 U (10 cm x 10 cm x 5 cm)
Power Consumption	3 W
Instrument Mass	1 kg
Altitude Range	250 - 450 km
Operational Life	660 days (1.8 years)
Mass Measurement Range and Resolution	0 - 60 AMU > 50 at 60 AMU
Spatial Resolution	10 km along-track sampling
Sensitivity for N_2	$>$ 8e-4 cps/(particles/cm^3)
Secondary Instrument Requirements	
Neutral Temperature Range	200 - 2500 K
Ion Temperature Range	250 - 2300 K
Signal-to-Noise Ratio	> 7
Particle Transmission Efficiency	50%

In the table above, "cps" means "counts-per-second" and "AMU" means "atomic mass units".

$$\text{Mass Resolution} = \frac{\text{mean arrival time}}{\text{2FWHM}} \tag{1.1}$$

Some secondary requirements for the MTOF-MS are also listed in Table 1.1. The temperature requirements are values predicted by current atmospheric models and will have an effect on the mass resolution and transmission efficiency of the instrument. The signal-to-noise ratio (SNR) requirement is necessary to ensure the validity of the lower end of the instrument measurement range. Transmission efficiency describes what percentage of the particles will successfully travel through the instrument.

1.2 Instrument Evaluation and Success

The success of the instrument design will be based primarily on the mass resolution, sensitivity, and measurement cycle time. These metrics are widely used to describe the performance of mass spectrometers and will best show the advantages of this design. The instrument component designs will be evaluated based on how they help (or hinder) the overall instrument design in meeting the requirements in Table 1.1. The expected performance

of the instrument can also be compared to expected values from the US Naval Research Lab Mass Spectrometer and Incoherent Scatter Radar (NRLMSISE-00) model or other atmospheric models. Data from a similar instrument on the California Polytechnic State University ExoCube mission may also be available for comparison. The finished MTOF-MS would be well-suited for deployment on a constellation mission to explore the thermosphere and ionosphere. Given that CubeSats have a lower launch cost and are more easily flown in constellations than sounding rockets or large satellites, this CubeSat instrument could allow for atmospheric studies with increased spatial resolution. Increased spatial resolution would provide data for multi-directional evaluation of aspects of the models which define lateral variations in atmospheric properties.

1.3 Atmospheric Modeling and Upper Atmosphere Density/Composition

Sophisticated modeling of Earth's atmosphere is an important part of atmospheric and near-space research. These models provide expected values of atmospheric qualities for a given time and location. Researchers working with these models are continuously seeking to improve their accuracy, especially when observing atmospheric reactions over small distances. A recently updated model, the NRLMSISE-00, contains improvements made largely from the inclusion of new atmospheric measurements [2]. The density and composition components of atmospheric models have been used in the past to calculate drag force on satellites and, conversely, satellite tracking has been used to evaluate the accuracy of atmospheric density models [3]. Improving the accuracy of these models would improve drag force and lifetime estimation for satellites.

Sounding rocket and large satellite missions have been used for previous mass spectrometer studies of the Earth's upper atmosphere. The instruments developed for these missions have sufficient measurement accuracy and mass resolution, but are larger and more difficult to launch than their CubeSat compatible counterparts. While the measurements from these missions have significantly improved our understanding of Earth's upper atmosphere, there are still gaps in our knowledge of the dynamics of the thermosphere and ionosphere that limit our ability to explain atmospheric behavior on certain spatial and temporal scales. A

CubeSat constellation would have superior spatial resolution and could potentially provide data to help answer some of these outstanding questions.

1.4 TOF-MS Technique

Mass spectrometry is the process of determining the chemical composition of a sample based on particle mass. TOF-MS measures the mass-to-charge ratio and quantity of charged particles in a given sample [4]. TOF-MS is a well-developed spectrometry technique and the implementation issues affecting resolution, sensitivity, and measurement cycle time are well known. This type of instrument determines particle mass based on a temporal data spectrum. Particles of varying mass are accelerated through an electric potential. This results in an increase in kinetic energy that causes the velocity of the particles parallel to the potential drop to be inversely proportional to the square root of the mass-to-charge ratio [4]. Higher velocities correspond to lower particle mass. The difference in velocities leads to differences in flight times through a fixed-length field-free drift region. The time of flight to the detector is measured and used to determine the particle mass. The relationship between particle mass and total flight time can be derived using Newtonian physics [4]. Often, ion mirrors, or reflectrons, are incorporated into TOF-MS designs. Reflectrons are devices made from a series of charged rings or grids, inside which a retarding electric field is created. Reflectrons can be used to redirect the particle flight paths or to correct for initial velocity distributions. Redirecting the particle flight paths can allow for longer flight times and better separation of different masses without increasing the length of the instrument [5]. Flight times depend on several factors, primarily the length of the field-free region through which the accelerated particles are allowed to drift and the speed at which the particles travel through the instrument.

1.5 Miniaturization of TOF-MS

Examples of miniature TOF-MS instrument designs have been simulated using SIMION and presented in the literature. One example is a 1 U TOF-MS SIMION experiment done at NASA Goddard Spaceflight Center (GSFC) in 2008. The GSFC team used SIMION

to build a virtual version of the instrument and simulate the electric fields that would be generated by the instrument electrodes. The instrument resolution and measurement range was determined by measuring particle flight times to a certain location in the instrument (where the detector would be placed) and evaluating the ratio between the width of the arrival time distribution for one mass and the difference in mean flight times between two adjacent masses for many different pairs of particle masses [6]. This simulation showed the theoretical feasibility of miniaturizing TOF-MS technology.

Miniaturization of this technology will result in faster particle flight times with smaller differences between masses due to much shorter drift spaces than traditional TOF-MS instruments. The length of drift regions can have significant effects on the resolution of the instrument, depending on which focusing techniques are used [4]. Particle flight times to the detector must be large enough that the detector performance characteristics do not completely degrade the separation between arrival times.

The accuracy of measurements taken by MTOF-MS could be affected by sample size (the number of particles used for each measurement). The aperture inlet to the instrument will need to be small to limit the width of the ion trajectory space and the size of particle samples. Charged grids, which are used to create more uniform electric fields, typically have transmission efficiencies of less than 90% [5]. Using too many charged grids may reduce sample size enough to degrade the instrument sensitivity.

Fortunately, miniaturization of some TOF-MS components may have benefits. Acceleration grids with smaller areas will have fewer charged wires and lower effective capacitance than larger grids. This lower capacitance may allow for faster rise/fall times for the grid pulses. Smaller components may also require less power to operate.

1.6 Sources of Instrument Performance Degradation

To meet the mass resolution requirement, the instrument needs to create a discernible and measurable difference in the arrival times for different masses. This will be accomplished by achieving a certain mean and width of arrival time distributions that are affected by many factors. These factors include the magnitude and direction of initial particle velocity

distributions, time-of-entry into the acceleration region, and non-ideal electric fields [4]. Particle samples will have a naturally occurring initial velocity distribution that will be visible in the particle detector data and can be mitigated using focusing techniques [7]. A spread can occur in the particle time-of-entry when a gating device is used; this time-spread will have a greater effect for instruments with smaller total flight times [4]. The incoming particle stream can be chopped using some low-power techniques, but an ideal delta pulse cannot be achieved. TOF-MS instruments that do not use permanent magnetic fields often have degraded resolution [8]. Perfect homogeneous electric fields cannot be built. Accelerating grids will come close to creating homogeneous fields, but there will still be inconsistencies that can cause deviations in flight paths of the ions [4]. Redirected trajectories may cause variation in detected flight times or a lower instrument sensitivity. Resolution may also be affected by the axial length of the ion detector or non-ideal dynamics in analog electronics used for detection [9].

Microchannel plate (MCP) detectors are commonly used in TOF-MS and are used as a detector for the preliminary design of this instrument. Another option for the instrument detector is discussed in Chapter 4. MCPs are small plates through which there are millions of electron multiplier channels of very small diameter (see Figure 1.1) [1]. The channels are charged when a voltage is applied between the two flat surfaces of the plate [1]. Each channel is between 10-100 μm in diameter and coated with a semiconducting material which emits secondary electrons when struck by incoming particles [1]. MCPs operate much like capacitors and thus have non-ideal characteristics such as dead time (time taken to recharge the semi-conducting walls of the channels) and time-of-response (time taken for the output signal to respond to an incoming particle [1]. Particle flight times must be sufficiently far apart to overcome the effects of these non-ideal properties on the detector output.

1.7 Ways to Improve Instrument Resolution

Although TOF-MS is subject to the above sources of mass resolution degradation, there are many techniques that have been developed to refine the measurement resolution of larger instruments that may be adapted for the MTOF-MS. Energy and velocity focusing

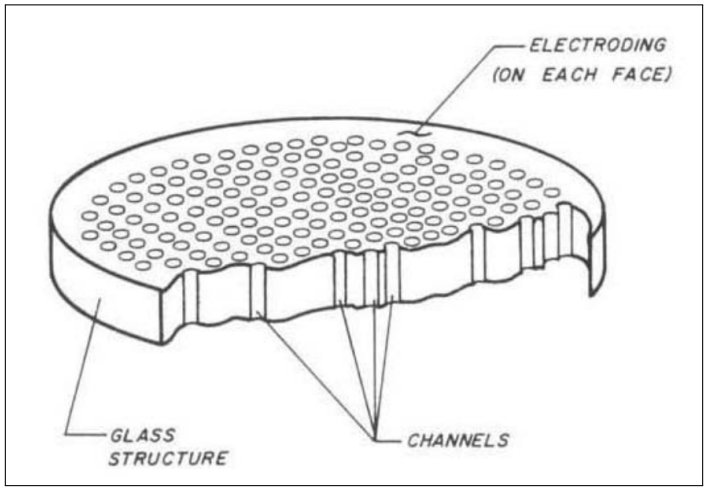

Fig. 1.1: Microchannel Plate Concept Drawing [1, Figure 1]

of ion packets using reflectrons or acceleration region variations is reported in the literature [7]. Using deconvolution of the detector response or gate pulse, if they are well known, could improve resolution by removing some detector or gating effects. Cross-correlation techniques for multiple ion packets could be used to increase the SNR of the overall output [9]. A higher SNR will help with identifying particles in low concentrations. A technique called pulsed extraction, where the application of extraction potentials is delayed for some time after particles have begun entering the extraction region, may improve resolution. Pulsed extraction can convert a time-of-birth (TOB) or time-of-entry distribution into a spatial distribution [8]. The initial spread of ions across the extraction area will have a distribution of initial energies, depending on where they are in the extraction region when the extraction potential is applied [7]. There are well-known techniques for focusing this type of distribution. Focusing of spatial distributions using carefully chosen dimension ratios for accelerator spacing, drift region length, and electric field ratios has been reported in the literature [10]. This technique may be limited by the minimum realistic spacing between accelerator grids. The effects of initial velocity and spatial distribution could be further mitigated by using higher acceleration voltages [7]. Each of these focusing techniques may improve the resolution of the instrument but may also make the instrument design more complex.

A reflectron could be used to redirect the particle flight paths to allow for additional drift space. This could help separate the average arrival times for each mass value. Reflectrons have been used in the past to improve resolution by correcting for spatial distributions [4]. A reflectron is made from a stack of charged rings (gridless reflectron) or a stack of charged grids (gridded reflectron). Gridless reflectrons have shown resolving power that is independent of ion beam divergence and may be better for measurements with varying starting conditions [5]. Since accelerator grids will block some portion of the particles passing through them, gridless reflectrons have a higher transmission efficiency than gridded reflectrons [5]. Transmission efficiency has a significant effect on the sensitivity of the instrument.

Many of the issues with particle distributions and non-ideal instrument electronics can be simulated in SIMION by adjusting the particle definitions for each simulation [11]. Variations in electric fields can also be simulated using SIMION, with accuracy depending on the parameters that are chosen for the potential array refinement [11].

1.8 MTOF-MS Design

The design of the MTOF-MS will include an aperture, an ionizer device, a gating device, initial and final accelerator grids, drift regions, a reflectron, and a detector device. Figure 1.2 shows a sample MTOF-MS design to demonstrate the instrument layout.

The aperture will allow samples of ions and neutral particles into the MTOF-MS. It will be covered during the satellite launch. The aperture design will limit the number of incoming particles with high off-axis velocity components.

The ionizer will be used to positively charge incoming neutral particles. There are several well-known techniques for particle ionization. An efficient, miniaturized ionizer for the MTOF-MS may already be available and will not be a focus of this research. If the design does not include an ionizer, MTOF-MS will still be capable of studying ion composition.

A Bradbury-Nielsen gate (BNG) will be used as a gating device for the MTOF-MS. A BNG is a series of alternately polarized parallel wires that create electric fields perpendicular to the ion flight paths. When the gate is charged, ions are deflected away from

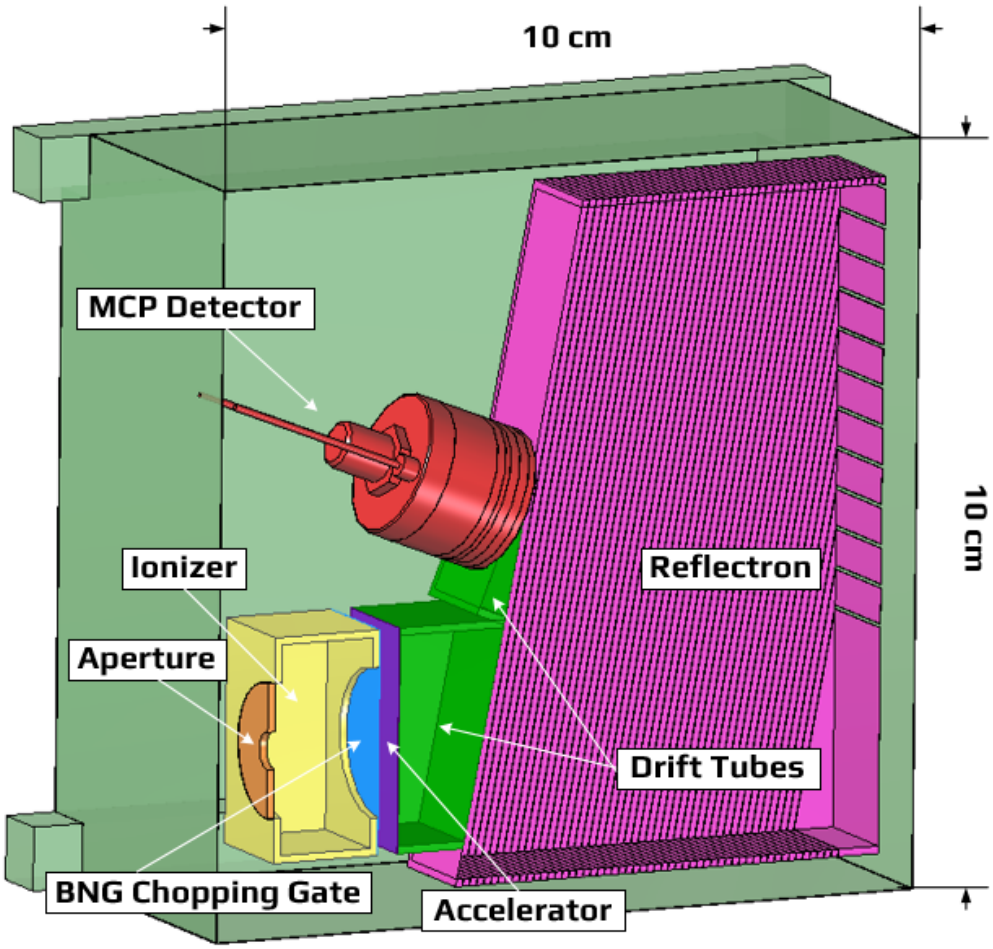

Fig. 1.2: TOF-MS Design Layout

the acceleration region [12]. When the gate is not charged, ions are allowed to fly straight through the gate. BNGs can be easily fabricated: SDL has fabricated BNGs for a sounding rocket TOF-MS and can provide the expertise and facilities to guide the development of a miniaturized version for this instrument [13].

The drift regions of the MTOF-MS will be field-free regions where the accelerated particles are allowed to separate by mass, as described in the literature. The dimensions of these regions will depend on the focusing techniques and the space constraints of the CubeSat. There will be two drift tubes, one between the acceleration grids and the reflectron entrance, and another between the reflectron entrance and the MCP detector.

The reflectron for MTOF-MS will be a series of rings with voltages applied to create

a retarding electric field. A gridless reflectron has much better transmission efficiency than a gridded, homogeneous field reflectron and may also provide off-axis focusing of the ion beam [5]. Voltages on the reflectron rings will be controlled using customized commercial resistor nets. The size of the reflectron will be limited by the dimensions of other components and the requirements of energy focusing techniques.

Additional acceleration may be required to ensure that particle energies are high enough that the detection efficiency of the MCP device is consistent across mass values. It has been shown that certain types of MCPs require between 3-5 keV to achieve a consistent efficiency across a range of particle masses [14]. Accelerating particles to speeds in this range before they fly through the instrument may not be practical due to the small drift space and a need for measurable flight times.

Charged particles will be detected by a commercially-supplied TOF MCP detector package. The detector will be chosen such that the electrical performance characteristics do not significantly degrade mass resolution and the holding voltages required for the detector plates are within the power constraints of the CubeSat.

If possible, this design will implement spatial focusing of particle distributions using three-stage acceleration. The technique requires specific ratios between the electric fields, accelerator spacing, and drift region length. This option will be explored using estimations of particle flight time through the instrument and, if successful, may be implemented in the final design. The practical minimum spacing between accelerators will require a specific drift length that may not fit within the instrument dimensions or may limit the space available for the reflectron.

1.9 Instrument Electronics

The performance of the physical components of the design will depend largely on the electronics design of the instrument. A layout of the instrument electronics is shown in Figure 1.3.

Some of the instrument electronics will be relatively easy to implement. For example, the voltage drivers for electrodes that will not be adjusted (such as the reflectron, drift re-

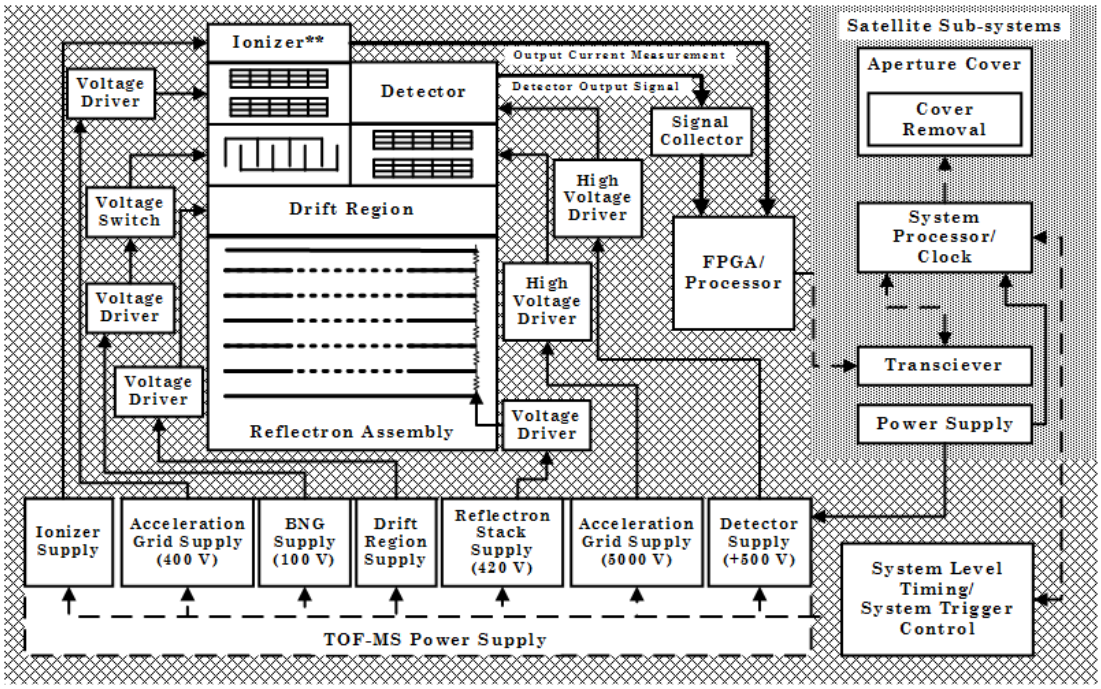

Fig. 1.3: TOF-MS Electronics Layout

gion, and acceleration grids) will require only voltage conversion. This research has focused on electronics for other components, including a switching voltage driver for the instrument gate and a signal collector for the instrument detector.

1.9.1 BNG Voltage Driver

The instrument gate and driver are described in Chapter 3 and summarized here. The gate efficiency depends mainly on the magnitude of voltage drop across the gate. The design analysis covered in Chapter 2 shows that instrument mass resolution degrades as the open time of the gate increases and that the open time should be kept to tens of nanoseconds. Therefore, operating the gate requires high voltage switching at very high speeds. Electronic drivers for this type of gate device have been built before. The design created for this project aimed to improve upon the voltage drop, open time, and output waveform characteristics of a previous design built at SDL.

1.9.2 MCP Detector Signal Collector

The instrument detector signal collector is described in Chapter 4 and summarized here. This circuit is designed to quantize the information from the MCP detector and create digital information about the particle arrivals. Due to the high variation in density in the upper atmosphere, the MCP output signal will indicate individual particle arrivals (where particles arrive far enough apart to appear as individual pulses from the MCP), a stream of overlapping particle arrivals (where particles arrive more closely spaced than the minimum pulse of the MCP detector), or some combination of the two. These two output signals would require different quantization and sampling techniques. The design for this project focuses on creating a signal collector for individual particle arrivals. The design presented in Chapter 4 leverages the consistent pulse shape for a single hit to the MCP detector and is intended to count pulses in certain time bins in order to roughly determine the mass spectra.

Chapter 2

Preliminary Design Analysis

The design of instrument payloads for space science missions is a complicated process. While TOF-MS technology is not a new area of study, the development of miniature-scale TOF-MS instruments for space and atmospheric research is relatively new. These instruments require several different components which will each have a different effect on the particle samples; in addition, there are different options for each component that may affect the performance of the instrument. Preliminary design analysis tools were developed to explore the challenges associated with the instrument design and help determine if the design goals are achievable. These include a tool to estimate the sensitivity of the instrument, a tool to estimate the instrument output, a dimension optimization tool to determine a starting point for the design, and a comparison of particle trajectories through the instrument with two different reflectron field shapes.

2.1 Sensitivity Estimation: Measurable Density Estimation Tool

The Measurable Density Estimation Tool (MDET) was developed to estimate the sensitivity of the instrument. The sensitivity to each type of neutral or ion is used to estimate the range of densities that can be reliably detected by the instrument using the detector system described in Chapter 4. The sensitivity of the instrument to each type of particle is calculated in a similar manner to the procedure described by King et al. in Section 3 of their paper [6]. A list of the inputs to MDET is shown in Table 2.1.

2.1.1 Sensitivity Calculation for Neutrals

The sensitivity to neutrals is calculated by first finding the ionizing efficiency ϵ_i as shown by King et al. [6], also shown in Equation 2.1. The ionizer current, j_i, is the current

Table 2.1: Inputs to Measurable Density Estimation Tool

Input Name	Description	Units	Variable or Fixed
Maximum and Minimum Altitude	Range of altitudes through which the instrument will fly. Also used to pull densities from atmospheric models for comparison	km	Fixed
Aperture Radius	Size of the instrument aperture through which the samples enter the instrument	cm	Variable
Gate Pulse Width	Amount of time the instrument gate is open	s	Variable
Measurement Cycle Time	Amount of time elapsed between the start of the gate pulse and final particle arrival	s	Variable
Spatial Resolution	Along-track distance over which measurements will be integrated	km	Fixed
Grid Transmission Efficiency	Percentage of particles in a sample that will be able to pass through each wire grid	unitless	Fixed
Number of Grids	Number of charged grids in the instrument through which samples will pass	grids	Fixed
Trajectory Efficiency	Percentage of particles in a sample whose trajectories through the instrument will allow them to impact the detector	unitless	Variable
Detector Efficiency	Percentage of particles which impact the detector that will actually create a pulse in the detector output signal	unitless	Fixed
Electron Current	Amount of current flowing from the ionizer filament during ionization	A	Variable
Detector Dark Counts	Number of false indications of particle arrival when the detector is not exposed to light	cps	Fixed
Noise from Light	Number of false indications of particle arrival caused by light hitting the detector	cps	Fixed
Desired Signal-to-Noise Ratio	Desired ratio between actual particle arrivals measured to false particle arrival measurements	unitless	Variable
Ionizing Electron Incident Energy	Energy at which the ionizing electrons will impact neutrals (depends on voltage applied to the ionizing device)	eV	Variable
Ionization Cross Section	Cross section for electron to impact a particle to ionize it	cm^2	Fixed

of electrons supplied by the ionizer and is an adjustable aspect of the design. The charge of one electron, e, is fixed. The path length of the ionization beam through the sample, l, depends on the width of the incoming neutral particle stream. The width of the particle stream is estimated to be 110% of the diameter of the aperture. The ionization cross section, σ, depends on the type of particle (which is fixed) and the energy of the incident electrons in the ionization beam (which is an adjustable part of the design).

$$\epsilon_i = \frac{j_i}{e} l\sigma \tag{2.1}$$

To calculate the sensitivity to neutrals, the ionization efficiency is multiplied by the transmission efficiency of the instrument ϵ_{tr}. The transmission efficiency calculation is shown in Equation 2.2. The trajectory efficiency, ϵ_t, is the percentage of particles entering the instrument which actually impact the detector. This value depends upon the ion optics of the instrument and is estimated to be 70%. The grid transmission efficiency, ϵ_g, is the amount of particles that will pass through the grid. The grid transmission efficiency depends on the thickness and spacing of the wires in the grid and is estimated to be 85% per grid. N is the number of grids in the design. The detector efficiency, ϵ_d is the percentage of particle hits indicated in the detector output and has been found to be 60% for particles at 3 keV [14].

$$\epsilon_{\text{tr}} = \epsilon_t \epsilon_g^N \epsilon_d \tag{2.2}$$

The sensitivity to neutrals, s_n is shown in Equation 2.3.

$$s_n = \epsilon_{\text{tr}} \epsilon_i \tag{2.3}$$

The sensitivity to ions, s_i, is calculated using the transmission efficiency, aperture size, and ram velocity and is shown in Equation 2.4.

$$s_i = \epsilon_{\text{tr}} v_{\text{ram}} A_{\text{aperture}} \tag{2.4}$$

2.1.2 Calculation of Measurable Densities

The sensitivity of the instrument is a standard for evaluating the performance of the instrument. This design has specific altitude requirements where the sample densities for each element are, however, roughly known. Although sensitivity does fully describe the range of the instrument, the MDET translates the sensitivity to a measurable density range for each constituent so that the instrument capability can easily be compared to the expected composition of the atmosphere (from atmospheric models).

For the minimum measurable density, MDET factors in the desired signal-to-noise ratio and noise from the detector. The detector noise is dependent on the type of detector. The MDET calculates the Minimum Counts Per Second (cps) as shown in Equation 2.5 and then the Minimum Measurable Density as shown in Equation 2.6.

$$\text{Minimum CPS} = (\text{Detector Dark Counts} + \text{Noise from Light})\text{SNR} \tag{2.5}$$

$$\text{Minimum Measurable Density} = \frac{\text{Minimum CPS}}{\text{Sensitivity}} \tag{2.6}$$

For the maximum measurable density, MDET factors in the operational characteristics of the particle detector. The particle arrivals are expected to be distributed across a window of time similar to the gate pulse width. The MDET assumes that, with detector output pulses about 1 ns in width, the maximum number of particles that can be confidently detected is half the width of the gate pulse (in ns). In other words, 2 ns of time should be reserved for each particle arrival (or a maximum of 50,000,000 cps). The MDET calculates Maximum Measurable Density as shown in Equation 2.7.

$$\text{Maximum Measurable Density} = \frac{\text{Maximum CPS}}{\text{Sensitivity}} \tag{2.7}$$

2.1.3 Conclusions from MDET Calculations

The minimum measurable densities were compared to $\frac{1}{10}$ of the minimum density from the MSIS atmospheric model over the desired altitude range. The maximum measurable

densities were compared to 10 times the maximum density from the same MSIS model over the desired altitude range. The calculations in the MDET show that measuring the range of expected densities throughout the desired altitude range is possible for most species, but only with the ability to adjust the current of ionizing electrons used in the ionizer. Although this is not ideal, adjusting the ionizer current to changes in the satellite altitude is a reasonable solution to achieve the needed measurement range, since the expected densities for each constituent all trend with altitude in the same way. As shown in a sample of the neutral atmosphere model in Figure 2.1, the density of each constituent increases as altitude decreases.

2.2 Mass Resolution Estimation: Flight Time Estimation Tool

The Flight Time Estimation Tool (FTET) was developed to estimate the instrument output. The FTET calculates arrival time distributions of particles. These estimated arrival time distributions can be used to estimate the mass resolution of the design.

The flight time of a particle through the instrument is based on some initial particle properties as well as the dimensions and electric potential of key parts of the design. A list of the FTET inputs is shown in Table 2.2.

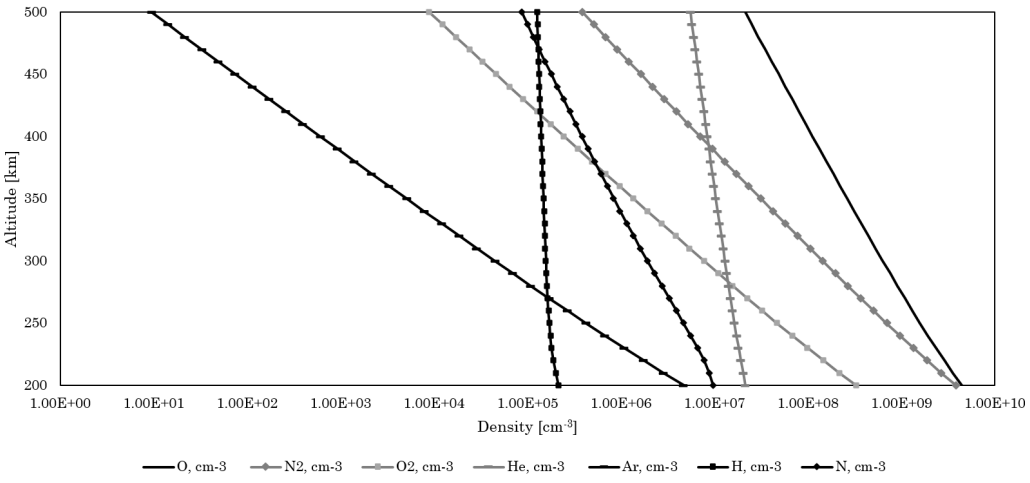

Fig. 2.1: Neutral Particle Densities vs. Altitude

Table 2.2: Inputs to Flight Time Estimation Tool

Input Name	Description	Units	Variable or Fixed
Particle Mass	Mass of particle being flown through instrument; identifies type of particle	AMU, kg	Variable
Temperature	Ambient temperature of atmosphere where sample is taken	$^{\circ}C$, $^{\circ}K$	Variable
Satellite Ram Velocity	Apparent speed of incoming particles caused by speed of satellite in orbit	m/s	Variable
Charge per Particle	Amount of electric charge; assumed to be 1 e	C	Fixed
Ionizer Length	Length of device to create electron beam, used to positively charge neutral particles	mm, m	Fixed
Acceleration Grid Thickness	Axial length of grid used to create acceleration regions	mm, m	Fixed
Acceleration Region Length	Spacing between two charged grids where particle acceleration happens	mm, m	Variable
Acceleration Potential	Difference between voltage levels applied to two adjacent acceleration grids	V	Variable
Gate Thickness	Axial length of grid used to separate incoming particle stream into discrete samples	mm, m	Fixed
Gate Pulse Width	Amount of time that the gate device of the instrument remains open	ns, s	Variable
Drift Region 1 Length	Length of field-free region where particles separate by mass	mm, m	Variable
Reflectron Depth	Depth of region where electric field is created to redirect particles towards detector	mm, m	Variable
Additional Reflectron Voltage	Additional total potential drop in the reflectron (added to the total acceleration potential to determine total potential difference in reflectron)	V	Variable
Drift Region 2 Length	Length of field-free region where particles separate by mass	mm, m	Variable

2.2.1 Fitting Instrument within the Volume Requirement

The instrument dimensions are calculated to fit within the $\frac{1}{2}$ unit volume listed in the instrument requirements, with $\frac{1}{2}$ cm of spacing left on each side to allow for mounting or satellite electrical harnesses. A few of the component dimensions are taken to be fixed values because they represent existing components that will be acquired for the instrument. The layout of the instrument dimensions is shown in Figure 2.2, and the equations used to constrain the instrument to the available volume are shown in Equations 2.8, 2.9, 2.11, 2.12, and 2.13. In Figure 2.2, $l_{\text{instrument}}$ is set at 100 mm (per the volume requirement) and $d_{\text{allowance}}$ is 5 mm. The variable d_{mcp} depends only on the choice of MCP detector for the instrument, d_e indicates the axial space required for the aperture and ionizer devices, ψ is the angle of the deflection of the particle trajectories within the reflectron, and l_g indicates the acceleration region length.

$$d_{\text{s1}} = 0.5OD_r \tan(\psi) \tag{2.8}$$

$$d_{\text{s2}} = \frac{d_r}{\cos(\psi)} \tag{2.9}$$

$$d_{\text{s3}} = 0.5W_{\text{mcp}} \tan(2\psi) \tag{2.10}$$

$$d_{\text{etot}} = d_e + l_g \tag{2.11}$$

$$d_{\text{ft1}} = l_{\text{instrument}} - 2d_{\text{allowance}} - d_{\text{etot}} - d_{\text{s2}} - d\text{s1} \tag{2.12}$$

$$d_{\text{ft2}} = \frac{l_{\text{instrument}} - 2d_{\text{allowance}}}{\cos(\psi)} - d_{\text{s1}} - d_{\text{s2}} - d_{\text{s3}} - d_{\text{mcp}} \tag{2.13}$$

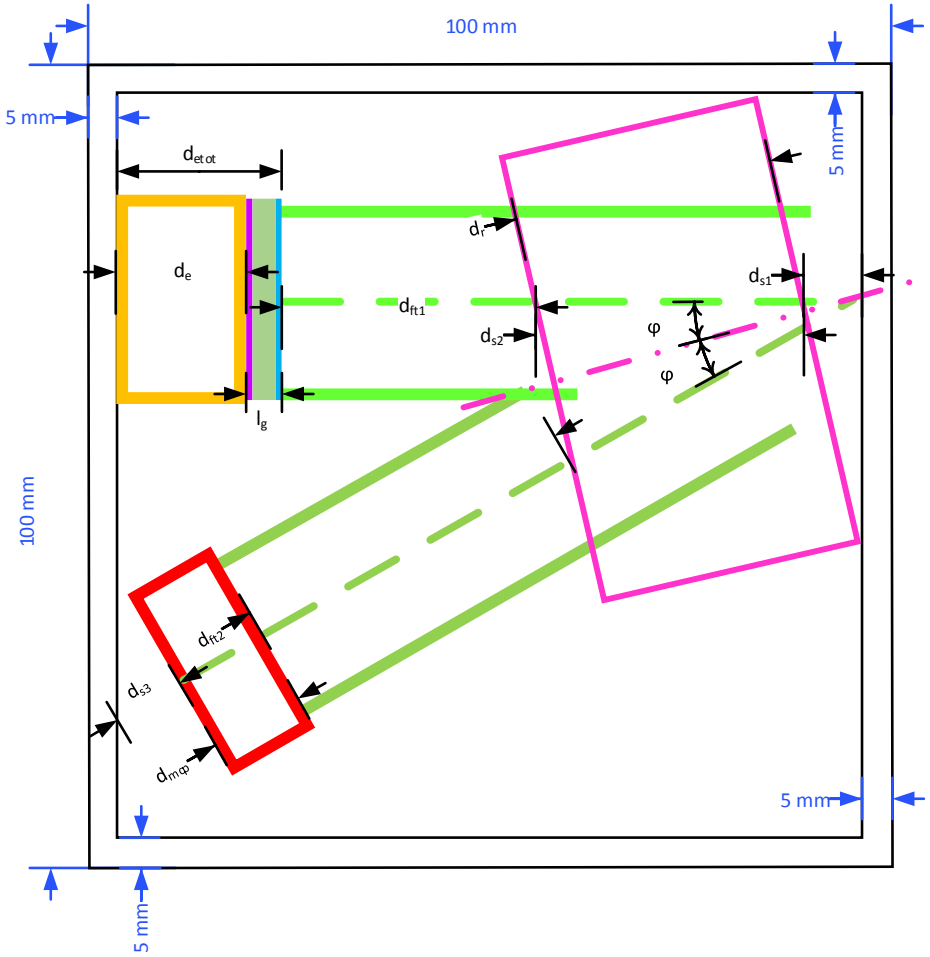

Fig. 2.2: TOF-MS Dimensions

2.2.2 Flight Time Estimations

The FTET calculates the flight time of one particle mass at a time by calculating the exit velocity and exit time for each section shown in Figure 2.3. The final flight time is a sum of the flight times through each component. The calculations are derived using Newtonian Physics and electrostatic acceleration; similar derivations for particle flight times in TOF-MS designs have been presented in the literature.

The FTET begins by calculating the initial state (mass, charge, and initial velocity) of a particle being flown through the instrument. The particle atomic mass is entered by the

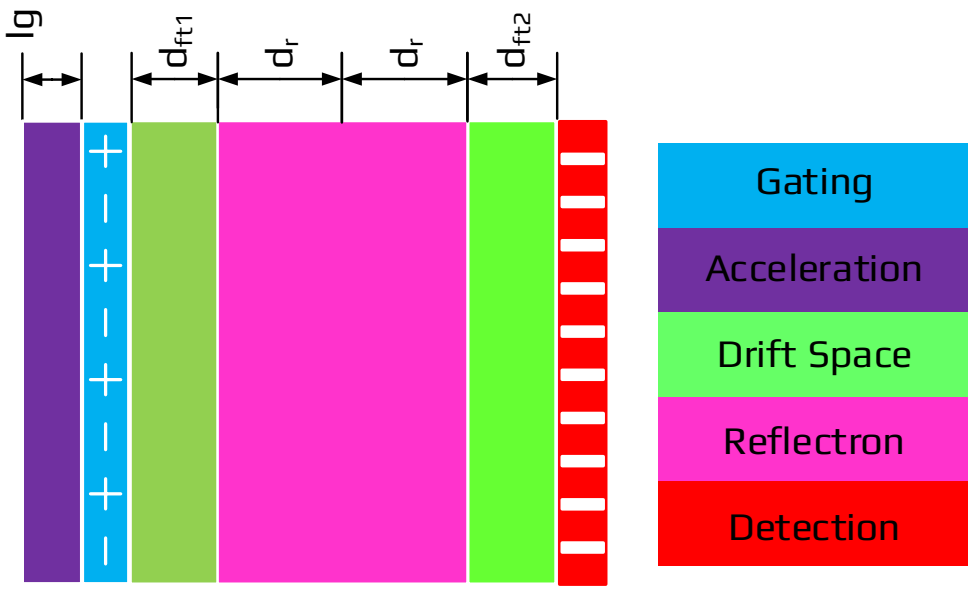

Fig. 2.3: Flight Time Estimation Sections

user and is converted to kg. Particles are assumed to be singly ionized. The initial velocity of the particle is entered as the satellite ram velocity. Since each sample of particles will have a naturally occurring distribution of initial velocities when entering the instrument that is a product of the thermal energy in the sample, the tool creates several representative cases within the particle distribution by calculating the thermal velocity for the sample and using this to find a range of possible initial velocities for the particle: mean, mean plus one, two, and three times the thermal velocity, and mean minus one, two, and three times the thermal velocity. The distribution parameter of the Maxwell-Boltzmann Distribution is used as the thermal velocity (see Equation 2.14) and is calculated from the particle mass (m, in kg), sample temperature (T, in $^\circ$ K), and Boltzmann constant (k, in J/$^\circ$K).

$$v_{\text{thermal}} = \sqrt{\frac{kT}{m}} \tag{2.14}$$

An ideal, delta pulse from the instrument gate device is not possible. Each sample taken by the instrument will have some distribution of arrival times caused by the finite about of time the gate is open. The gate pulse width, or open time, can be minimized, but not eliminated. To simplify calculations for the FTET, the distribution of start times is assumed to be uniform and to not extend beyond the time when the gate is closed. The gate open time is added to the flight time of the mean velocity particle and the particles with initial velocity at the slower first, second, and third standard deviations. This demonstrates the maximum spread in arrival times caused by the gate pulse width.

Two values are calculated for the acceleration region(s): the time it takes the particle to travel through the region and the final velocity of the particle as it exits. The equation of motion (EOM, Equation 2.16) for the particle calculates the increase in energy applied to the particle by the electric field in the acceleration region (E_f, Equation 2.15), assuming this field is uniform throughout the acceleration region. The particle velocity as it enters the acceleration region (v_{entry}), the acceleration potential drop (V_a), and the particle mass (m) are key inputs to the particle EOM. The acceleration potential drop is an adjustable variable in the instrument design. The entry velocity comes from the particle initial velocity, a function of the satellite ram velocity and the thermal velocity. The EOM is solved for the time (t_{exit}) at which the particle reaches the end of the region (Equation 2.17) by substituting the length of the acceleration l_g region for $x(t)$ and the velocity (v_{exit}) of the particle after acceleration (Equation 2.18) by substituting t_{exit} for t.

$$E_f = \frac{V_a}{l_g} \tag{2.15}$$

$$x(t) = E_f \frac{q}{2m} t^2 + v_{\text{entry}} t^2 = \frac{V_a}{l_g} \frac{q}{2m} t^2 + v_{\text{entry}} t \tag{2.16}$$

$$t_{\text{exit}} = \frac{-v_{\text{entry}} \pm \sqrt{v_{\text{entry}}^2 + \frac{2qE_f x(t_{\text{exit}})}{m}}}{\frac{qE_f}{m}} = \frac{-v_{\text{entry}} \pm \sqrt{v_{\text{entry}}^2 + \frac{2qE_f l_g}{m}}}{\frac{qE_f}{m}} \tag{2.17}$$

$$v_{\text{exit}} = v_{\text{entry}} + \frac{qV_0}{x(t_{\text{exit}})m} t_{\text{exit}} = v_{\text{entry}} + \frac{qV_0}{l_g m} t_{\text{exit}} \tag{2.18}$$

Flight time and velocity calculations for the drift regions are relatively simple. The flight time through a field-free region of length l_d is calculated using (Equation 2.19), where no external forces are acting on the particle. The entry velocity is the same as the exit velocity for the previous section (v_{exit} from the acceleration region). The exit velocity is taken to be the same as the entry velocity, since no acceleration is being applied to the particle in this region.

$$t_{\text{exit}} = \frac{l_d}{v_{\text{entry}}} \tag{2.19}$$

In the reflectron, the particle exchanges kinetic energy for potential energy as it travels towards the back of the reflectron. The particle is then redirected and accelerated back towards the opening of the reflectron. First, Equation 2.20 is used to describe the magnitude of the electric field at any point in the reflectron ($E_f(x(t))$). Equation 2.20 depends on two design variables, the maximum strength of electric field in the reflectron ($E_{\max}$) and the depth or axial length of the reflectron component (d_r). $E_{\max}$ is determined as in Equation 2.15, where V_0 is the difference between the potential on the first and last reflectron electrodes and l_g is replaced with d_r. Equation 2.20 describes what will be referred to as a quadratic-shaped electric field.

$$E_f(x(t)) = \frac{E_{\max} x^2(t)}{d_r^2} \tag{2.20}$$

The field in the reflectron opposes the particle's direction of flight, so the particle decelerates as it flies into the reflectron. The particle's kinetic energy is exchanged for potential energy as it flies into the decelerating field. Assuming that no total energy is lost, the distance the particle will travel into the reflectron is given by Equation 2.22 using this exchange of energy. The entry velocity is the exit velocity from the previous region (v_{exit} from the drift region).

$$x(t) = v_{\text{entry}} \left(\frac{\sqrt{d_r m}}{\sqrt{2qE_{\max}}} \right) \sin \left(\frac{\sqrt{2qE_{\max}}}{\sqrt{d_r m}} t \right) \tag{2.21}$$

$$v(t) = \frac{d}{dt} x(t) = v_{\text{entry}} \cos \left(\frac{\sqrt{2qE_{\max}}}{\sqrt{d_r m}} t \right) \tag{2.22}$$

The time it takes for the particle to come to a stop at the back of the reflectron (t_{stop}) can be found using the fact that $v(t)$ when the particle stops is 0 (or $v(t_{\text{stop}}) = 0$). The particle velocity, $v(t)$, is a cosine function, so $v(t) = 0$ when the cosine argument is $\frac{\pi}{2}$ (see Equation 2.23). The FTET assumes that the acceleration of the particle as it exits the reflectron mirrors the deceleration profile as it enters so that the total amount of time the particle spends in the reflectron (t_{exit}) can be calculated as twice the time taken for deceleration (see Equation 2.24). This assumes that the field in the reflectron only affects the speed of the particle in the axial direction and that the speed of the particle when leaving the reflectron is the same as when it enters.

$$t_{\text{stop}} = \frac{\pi^2 \sqrt{d_r m}}{\sqrt{8qE_{\max}}} \tag{2.23}$$

$$t_{\text{exit}} = 2t_{\text{stop}} \tag{2.24}$$

The arrival time of the particle is measured when it hits the MCP detector. Therefore, the arrival time of the particle is calculated by summing the flight times calculated for each of the previous regions. This includes flight times for the acceleration region (t_{accel}, Equation 2.17), first drift region (t_{drift1}, Equation 2.19), the reflectron (t_{reflect}, Equation 2.24), and a second drift region (t_{drift2}, Equation 2.19, where v_{entry} is the exit velocity from the reflectron).

$$t_{\text{arrival}} = t_{\text{accel}} + t_{\text{drift1}} + t_{\text{reflect}} + t_{\text{drift2}} \tag{2.25}$$

$$t_{\text{arrival}} = -\left(\frac{ml_g}{qV_a}\right) v_{\text{initial}} + \frac{d_{\text{ft1}} + d_{\text{ft2}}}{\sqrt{v_{\text{initial}}^2 + \frac{2qV_a}{m}}} + \left(\frac{ml_g}{qV_a}\right)\sqrt{v_{\text{initial}}^2 + \frac{2qV_a}{m}} + 2\frac{\pi^2\sqrt{d_r m}}{\sqrt{8qE_{\max}}} \quad (2.26)$$

2.2.3 Assumptions Used to Simplify FTET

The output of the FTET is based on several assumptions about the operation of the instrument or the spacecraft bus that would eventually carry the instrument. An allowance of 0.5 cm of spacing is reserved in each aspect of the volume restriction to ensure that the instrument can be fit in the spacecraft bus along with mounting, electrical harnesses, or other critical components. Calculations of particle acceleration are based on the assumption that the instrument electrodes will create ideal, uniform electric fields. In the acceleration and drift regions of the instrument, this assumption is valid since the field fringing effects in those regions will be negligible. In the reflectron portion of the instrument, the fields will be non-uniform with respect to the distance to the reflectron walls. The effect from non-uniform fields in the reflectron component of the instrument will be evaluated using the charged particle flight simulator, SIMION. The non-ideal fields may affect the instrument sensitivity but are not expected to significantly alter estimations of particle flight times or instrument resolution.

Furthermore, the assumption of uniform fields can still be used for flight time estimation because the wall voltages can be adjusted to achieve the desired potentials along the axis of the instrument. The main effect of non-uniformity in the reflectron field will be in shaping the trajectory of the particles as they exit towards the detector.

2.3 Comparing FTET Results to Ion Flight Simulation

The FTET is meant to quickly estimate the performance of a design in one dimension. A powerful ion optics simulator, called SIMION, already exists to allow evaluation of a design in multiple dimensions. To validate both the FTET results for a single design and the design optimization results, the flight times from the FTET were compared to flight times generated in SIMION. Components for an instrument with identical dimensions in

the axial direction (used in the FTET) were built using 3D modeling and imported as electrodes into the SIMION software. Particles with the same initial properties as used for the FTET calculations were flown through the instrument simulation and the flight times to the detector were measured. Partial flight times (flight times through each individual part of the instrument) were also measured and compared to FTET. The conditions for the simulation and FTET are listed in Table 2.4 and the results are listed in Table 2.3.

Figure 2.4 is a plot comparing the FTET output to a SIMION simulation using the same instrument dimensions and electrode voltages. For this experiment, FWHM is taken as the difference between the arrival times for two specific particles: the particle with less than 7 km/s initial velocity and greater than 0 ns TOB, and the particle with greater than 7 km/s initial velocity and 0 ns TOB. The data show a 17% decrease in mass resolution when the conditions used for FTET are applied to SIMION (68.0 $\frac{s}{\Delta s}$ vs 56.6 $\frac{s}{\Delta s}$, both at 60 AMU). The overall measurement cycle increases by 2% but the peak width increases by 18%.

There is some discrepancy between the FTET and SIMION. This discrepancy is an expected effect of the non-ideal field calculations in the SIMION tool and the FTET can

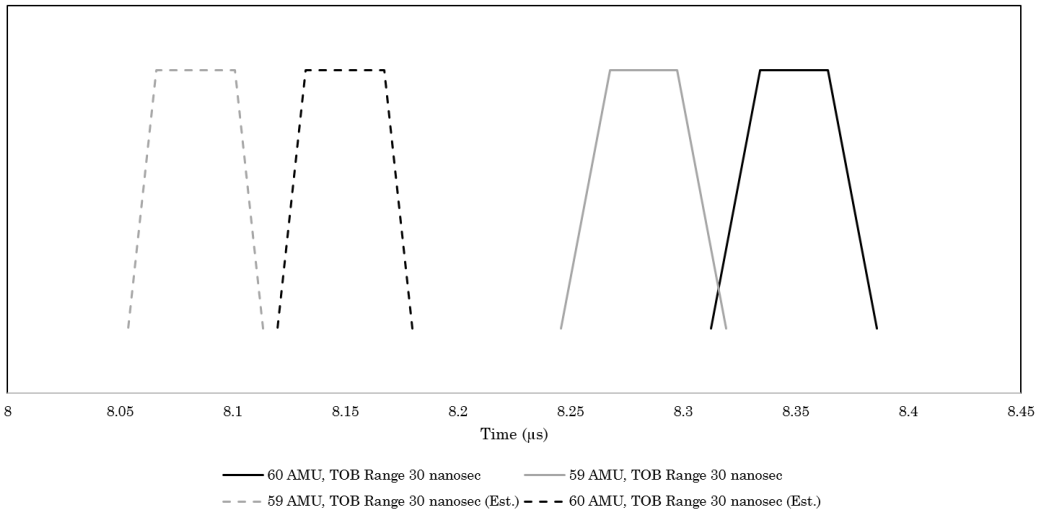

Fig. 2.4: Comparison of FTET and SIMION output for 59 and 60 AMU
The arrival times shown in this plot correspond to the data shown in Table 2.3. Dotted lines represent FTET data. Solid lines represent SIMION data. Both the simulation and estimation times were calculated using the conditions listed in Table 2.4.

Table 2.3: SIMION and FTET Data for Instrument Described in Table 2.4

Particle Mass Number	Start Velocity	TOB	Arrival Time	Source
60 AMU	7419.9 $\frac{m}{s}$	0 ns	8.3122 μs	SIMION
60 AMU	7419.9 $\frac{m}{s}$	0 ns	8.1199 μs	FTET
60 AMU	7000 $\frac{m}{s}$	0 ns	8.3342 μs	SIMION
60 AMU	7000 $\frac{m}{s}$	0 ns	8.1323 μs	FTET
60 AMU	7000 $\frac{m}{s}$	15 ns	8.3492 μs	SIMION
60 AMU	7000 $\frac{m}{s}$	30 ns	8.3642 μs	SIMION
60 AMU	7000 $\frac{m}{s}$	30 ns	8.1673 μs	FTET
60 AMU	6580.1 $\frac{m}{s}$	30 ns	8.38591 μs	SIMION
60 AMU	6580.1 $\frac{m}{s}$	30 ns	8.1799 μs	FTET
59 AMU	7423.5 $\frac{m}{s}$	0 ns	8.2457 μs	SIMION
59 AMU	7423.5 $\frac{m}{s}$	0 ns	8.0537 μs	FTET
59 AMU	7000 $\frac{m}{s}$	0 ns	8.2675 μs	SIMION
59 AMU	7000 $\frac{m}{s}$	0 ns	8.0660 μs	FTET
59 AMU	7000 $\frac{m}{s}$	15 ns	8.2825 μs	SIMION
59 AMU	7000 $\frac{m}{s}$	30 ns	8.2975 μs	SIMION
59 AMU	7000 $\frac{m}{s}$	30 ns	8.1010 μs	FTET
59 AMU	6576.5 $\frac{m}{s}$	30 ns	8.3190 μs	SIMION
59 AMU	6576.5 $\frac{m}{s}$	30 ns	8.1135 μs	FTET

Table 2.4: Conditions for Estimated and Simulated Flight Times in Table 2.3

Parameter	Value
Total Acceleration	153 V
Reflectron Depth	55 mm
Flight Tube 1 Length	6.1 mm
Flight Tube 2 Length	6.4 mm
Accelerator Spacing	3 mm
Number of Acceleration Grids	3
Acceleration Per Grid	51 V
Satellite Ram Velocity	7000 $\frac{m}{s}$
Temperature	1000 $^{\circ}C$
Additional Voltage in Reflectron	35 V
Gate Pulse Width	30 ns

still be used to evaluate individual designs. The estimations produced by the FTET were in agreement with SIMION through the acceleration regions and drift spaces, and were slightly faster than SIMION in the reflectron region, making the final flight times from FTET slightly faster. The difference in the reflectron flight times can be attributed to the assumption of ideal fields in the reflectron. SIMION does not use the assumption that the fields in the reflectron are almost uniform, and instead calculates the fields self-consistently given the voltages applied to the reflectron electrodes. As a result, the field magnitude in the reflectron region varies with distance to the reflectron walls and the potentials along the particle flight paths through the instrument are somewhat lower than those applied to the walls. Traveling through lower potentials, the particles can fly farther into the reflectron and take more time to turn around and exit the region. The electrode voltages could be tuned in the simulation to achieve flight times and mass resolution even closer to those of the FTET.

Even with slight disagreements in flight times in the reflectron regions, both SIMION and FTET show about the same estimation of measurement quality. Particles representing the initial velocity distributions and gate pulse width arrive in roughly the same patterns in both SIMION and FTET. Therefore, the agreement with SIMION validates the calculations in the FTET.

SIMION is a powerful tool through which many of the effects causing mass resolution degradation can be modeled. However, the FTET is a better tool for choosing dimensions because the calculations are much faster than the full ion simulation but yield similar flight time results. While the FTET cannot model the instrument as realistically as SIMION, it can be used to quickly compare different instrument designs. This ability is crucial to optimize the instrument design within the volume constraint.

2.4 Dimension Optimization Using FTET Results

The equations from Section 2.2.1 and Section 2.2.2, used to build the FTET, were subsequently used to find sets of optimized component dimensions. An optimization program was built using MATLAB software and included calculations for dimension fitting and flight

time estimation. The program uses a local search method to find a local maximum of an objective function based on the instrument mass resolution at 60 AMU (Equation 2.27) and the peak spacing at 59 and 60 AMU (Equation 2.28). The high-level program is shown in Algorithm 2.1 and the program code is included in Appendix A.

$$m_{\text{res}} = \frac{t_{60}(v_{\text{initial}} = v_{\text{ram}})}{2(t_{60}(v_{\text{initial}} = v_{\text{ram}} - v_{\text{th}}) - t_{60}(v_{\text{initial}} = v_{\text{ram}} + v_{\text{th}}))} \tag{2.27}$$

$$spacing = t_{60}(v_{\text{initial}} = v_{\text{ram}}) - t_{59}(v_{\text{initial}} = v_{\text{ram}}) \tag{2.28}$$

Practical limits were set for each of the inputs and the program was started from several different input sets to determine if the results were local or global maxima.

From each starting point, the program tended towards maximizing the reflectron depth and acceleration voltages. The first program included three acceleration regions and a variable ratio of the magnitude of the third region to the first region (the first and second regions were of equal magnitude, as described by Yildirim et al. [10]). Each time the voltage ratio was maxed out.

A second program written for an instrument with a single accelerator yielded better mass resolution values than a design with multiple accelerators and the same total acceleration voltage. The hypothesis that the volume restriction did not allow for multiple accelerator focusing to be accomplished is correct, with the effects of increasing the reflectron depth having a more positive effect on resolution than the large drift space required for accelerator focusing.

2.5 Reflectron Field Shapes and Particle Trajectories

The electrode voltage progression in the reflectron electrodes determines the shape of the electric fields within the device. In a gridless reflectron, variation in the electric field can cause undesirable changes in the particle trajectory through the instrument. If the change in particle trajectory pulls particles away from hitting the detector (reducing the trajectory efficiency), the instrument sensitivity will be reduced. A field with potentials

Algorithm 2.1 Dimension Optimization

Input:

Reflectron Depth (d_r)
Accelerator Spacing (l_g)
Acceleration Voltage (V_a)
Initial Velocity (v_{initial})
Ambient Temperature (T)
Upper Limit for Mass Range (60 AMU)
Maximum and Minimum Limits on Acceleration Voltage
Maximum and Minimum Limits on Reflectron Depth
Maximum and Minimum Limits on Accelerator Spacing

Output:

Spacing Value
Mass Resolution (at 60 AMU)
Peak Separation (between 59 and 60 AMU)
Optimized Acceleration Voltage (V_a)
Optimized Accelerator Spacing (l_g)
Optimized Reflectron Depth (d_r)
Optimized Flight Tube Lengths (d_{ft1} and d_{ft2})
Flight Time of 60 AMU in Optimized Instrument (tf_a)

Begin

Calculate thermal velocity v_{th}
Calculate flight tube 1 and flight tube 2 lengths from l_g and d_r
Calculate mass resolution m_{res} of starting dimensions
Do
Begin
Calculate surrounding dimension sets, $\text{dimension}_n \pm \text{stepvalue}$
Calculate mass resolution m_{res} for each surrounding set
Identify set with highest mass resolution (including starting point)
Set with highest mass resolution becomes new starting point
End
while Mass resolution of starting point is less than that of any of surrounding dimension sets

End

***Subroutine: Mass Resolution and Peak Spacing**

Calculate flight time for 60 AMU at ram velocity, tf_a
$v_{\text{initial}} = v_{\text{ram}}$
Calculate flight time for 60 AMU for distribution, tf_l and tf_h
$v_{\text{initial}} = v_{\text{ram}} \pm v_{\text{th}}$
Calculate flight time for 59 AMU at ram velocity, tf_{prev}
Calculate mass resolution
$m_{\text{res}} = \frac{\text{tf}_a}{2(\text{tf}_l - \text{tf}_h)}$
Calculate peak spacing
$\text{spacing} = \text{tf}_a - \text{tf}_{\text{prev}}$

End Subroutine

defined using a quadratic relationship between the depth in the reflectron and the voltage was chosen because of its capability to improve the resolution of the instrument. The field can be configured in different ways, depending on how the electrode voltages are chosen. Two different quadratic fields, shown in Figure 2.5, were tested in SIMION to evaluate their effects on the sensitivity of the instrument. Each of the two fields has the same change in potential between the first and last electrodes. They were named “quadratic” and “flipped quadratic” for the purpose of the evaluation. Table 2.5 shows the voltages applied to a 13 ring box reflectron (shown in Figure 2.6) in SIMION.

Figures 2.7 and Figure 2.8 show the resulting particle trajectories for particles fired straight into the instrument with no cross velocity distribution. The flipped field does a better job of keeping the particles traveling towards the detector along the width of the reflectron, but still allows the trajectories to spread along the bottom length of the reflectron box. The quadratic field spread the particle trajectories and decreases the trajectory efficiency in both directions. The flipped field was tested with the particle starting point in different places along the top of the reflectron box to see if the proximity to the walls affected the spread of particle trajectories along the bottom length of the box. No signif-

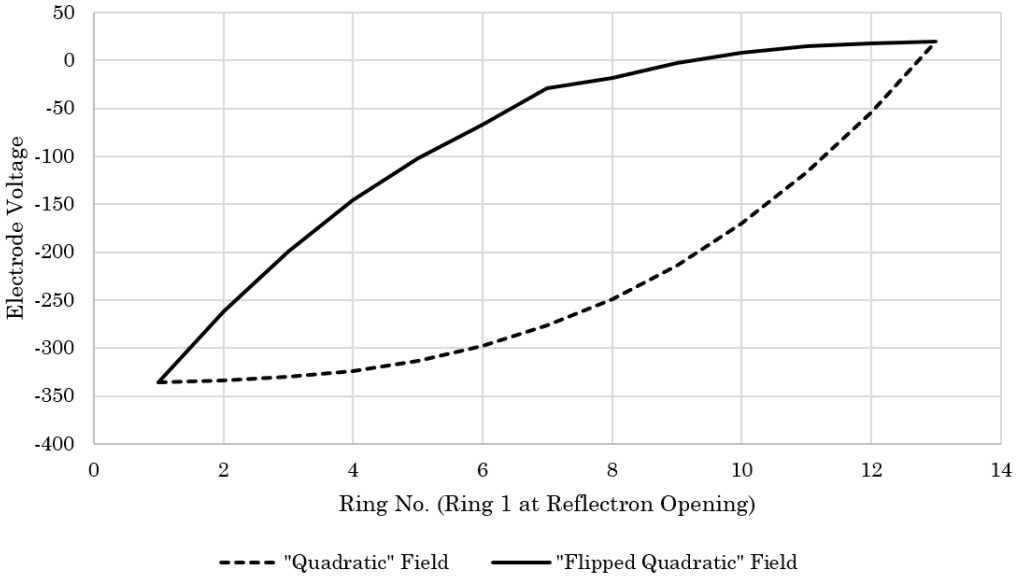

Fig. 2.5: Reflectron Field Shapes Tested for Trajectory Efficiency

Table 2.5: Electrode Voltages used in Reflectron Field Shape Evaluation

Quadratic Field		Flipped Quadratic Field	
Ring Number	Voltage	Ring Number	Voltage
1	-336	1	-336
2	-334	2	-262
3	-330	3	-199
4	-324	4	-146
5	-313	5	-102
6	-298	6	-67
7	-276	7	-29
8	-249	8	-18
9	-214	9	-3
10	-170	10	8
11	-117	11	15
12	-54	12	18
13	20	13	20

icant effect is seen, indicating that the results might be similar for a v-shaped reflectron with rectangular electrode rings. These results indicate that the "flipped quadratic" field should be used for the final design over a "quadratic" field.

2.6 Conclusions Based on Design Analysis

Following SIMION validation of the FTET, the estimations were used to observe the effect of a non-ideal gate pulse on an optimized instrument design. The optimized dimensions were tested with both a zero open-time gate (delta pulse) and a more realistic finite open-time gate (pulse width of 35 nanoseconds). Comparing the results from these two estimations showed that devices with real gate pulse widths significantly limit the performance of the instrument (see the FTET output in Figure 2.9 and the simulated spectra in Figure 2.10 comparing the particle arrival times for each situation). This result led to the focus of the design project on a voltage driver for a BNG intended to minimize the open-time (or pulse width) of the device.

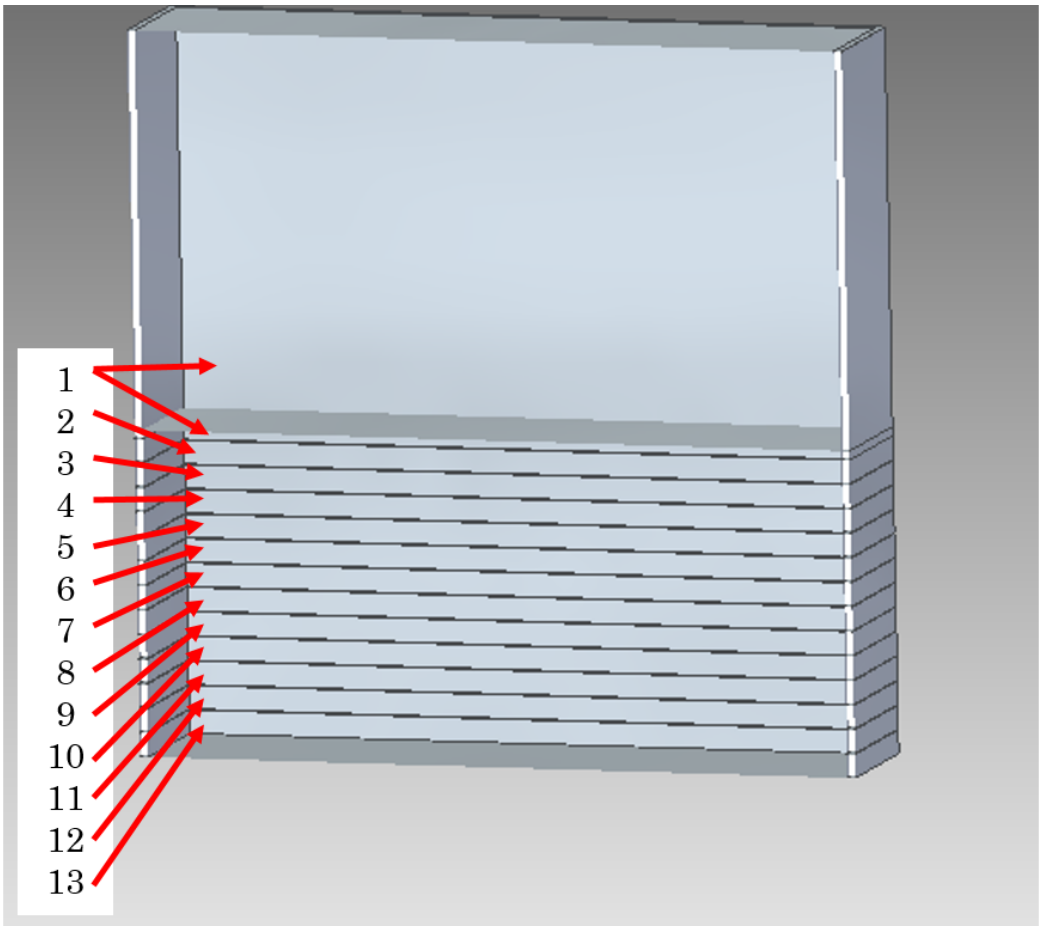

Fig. 2.6: 3D Model of Box Reflectron used for Field Shape Evaluation

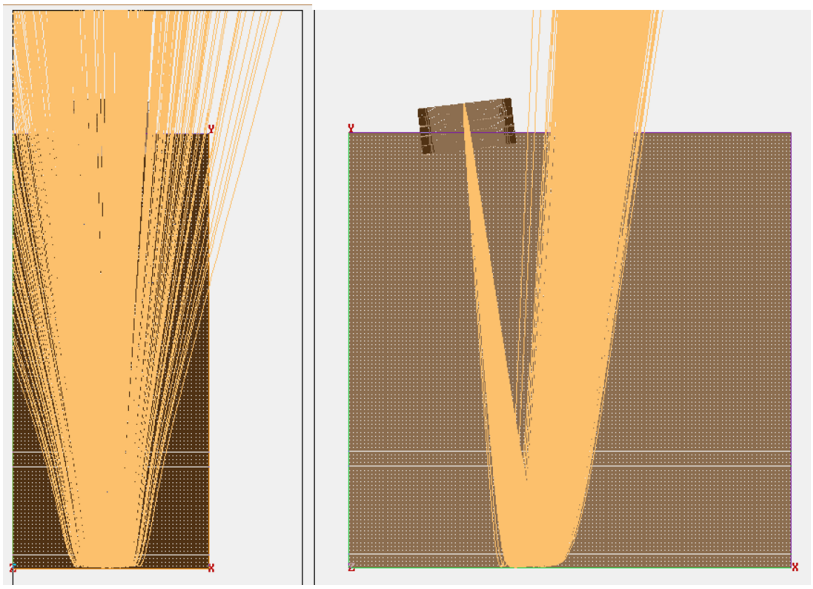

Fig. 2.7: SIMION Particle Trajectory Results for "Quadratic" Shaped Field
The simulation shows that this field shape will cause particle trajectories to spread away from the detector in two directions, lowering the trajectory efficiency of the instrument.

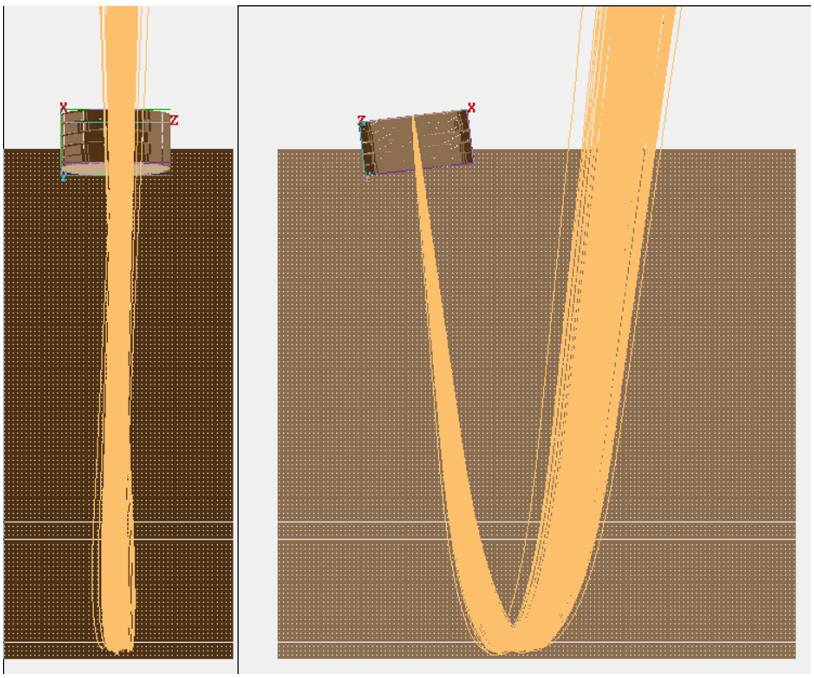

Fig. 2.8: SIMION Particle Trajectory Results for "Flipped Quadratic" Shaped Field
The simulation shows that this field shape will keep particle trajectories from spreading away from the detector in one direction, so it has a less negative effect on the trajectory efficiency of the instrument than the quadratic field.

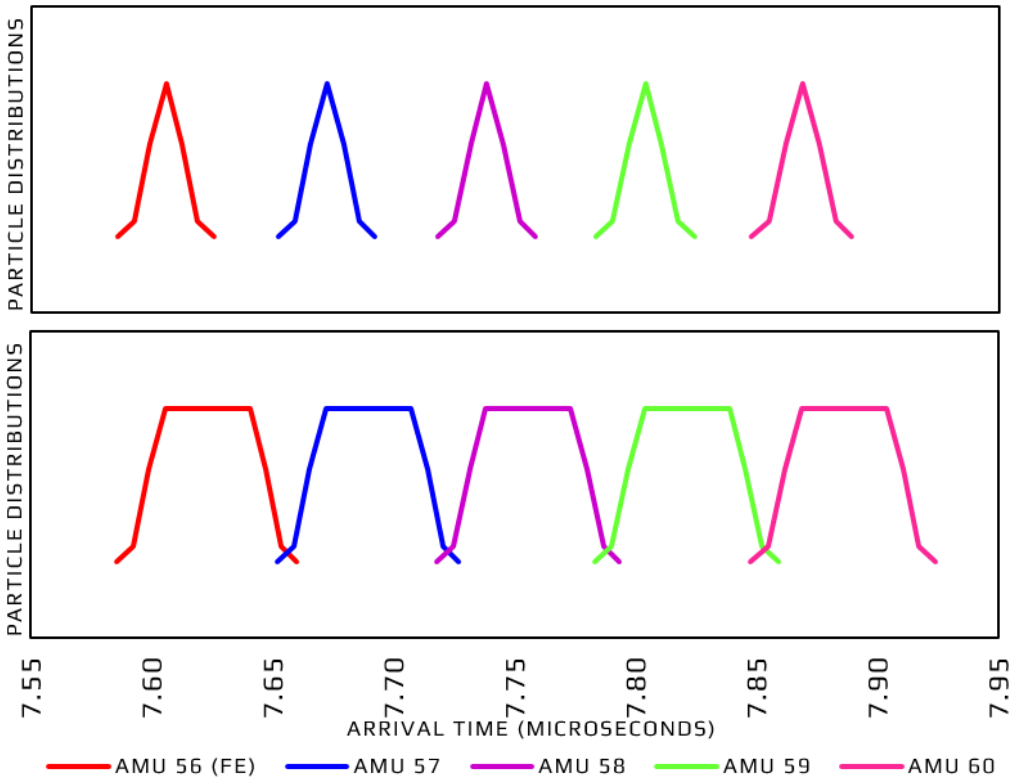

Fig. 2.9: Arrival Times with Ideal Gate vs. Real Gate

The figure compares the FTET output for an instrument with an ideal gate pulse of 0 ns (top plot) to a practical gate pulse of 30 ns (bottom plot). The plots show output directly from the FTET. The FTET plots are set up to roughly demonstrate the width of the arrival time distribution and are not shaped to match what the actual instrument spectra will look like.

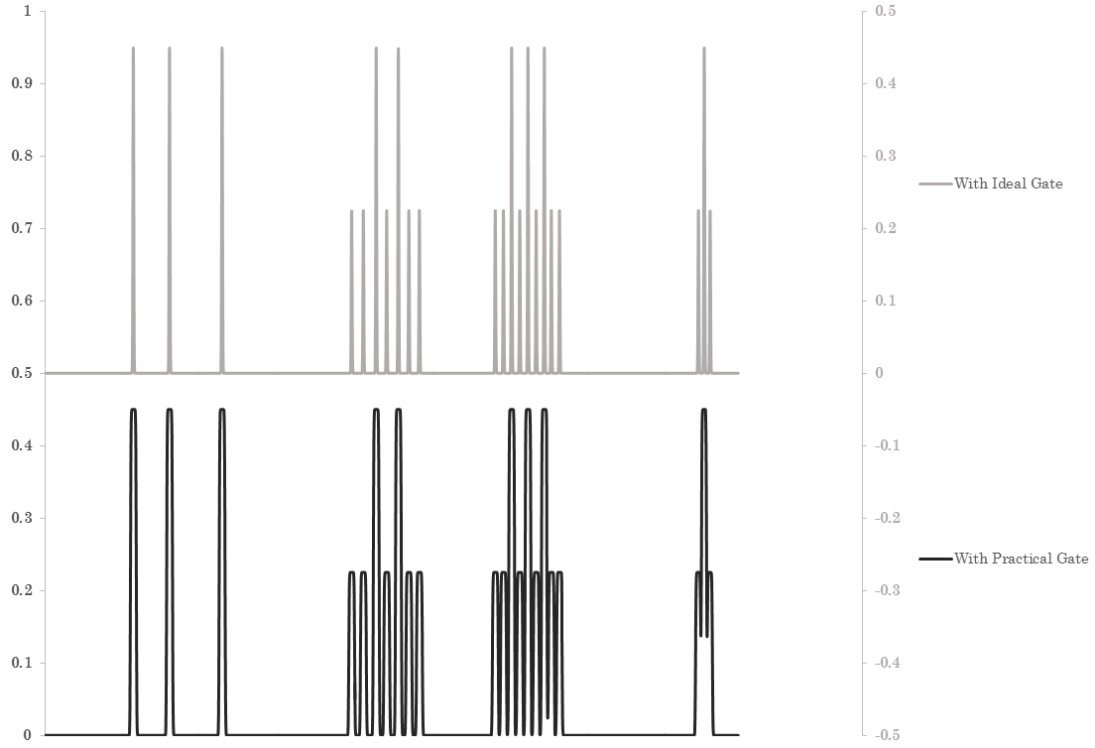

Fig. 2.10: Simulated Spectra with Ideal vs. Practical Gate Pulses
The plot shows a simulated spectra containing equal amounts of each of the atmospheric constituents from MSIS. Smaller peaks represent mass values of 1-2 AMU more or less than those of the common atmospheric constituents. Mean arrival times used to create this plot were calculated using FTET.

Chapter 3

BNG Switching Voltage Driver

3.1 BNG Driver Design

Preliminary design analysis reveals that the open time for the instrument gate device is a limiting factor for the instrument mass resolution. The amount of time the gate remains open (the gate pulse width) creates a distribution in the start times of particles in a sample. The distribution in start times directly affects the arrival time distributions for that sample. In order to maximize the instrument mass resolution, the gate pulse width needs to be minimized. The instrument design uses an electronic gating technique, so a high-speed, high-voltage driver is required.

3.2 BNG vs. Parallel Plate Gates

The gating device for this instrument is a BNG. This device is created using two sets of charged parallel wires. The wires are stacked such that every other wire belongs to the same set. An independent voltage is applied to each of the two sets. One set will be referred to as the "high" side of the gate and the other will be referred to as the "low" side. The operation of the gate is illustrated in Figure 3.1. When the gate is "ON", both sides of the gate are charged to the same potential and charged particles fly undisturbed through the gate. When the two sides are charged to different potentials, an electric field is created between the wires. This field is oriented perpendicular to the axis of the instrument and applies a force to charged particles flying through the gate. This force deflects particle velocity away from the axis of the instrument so that the particles are no longer traveling toward the detector. These particles never impact the detector and are never counted, so the instrument is effectively "OFF" even though particles continue to enter the aperture.

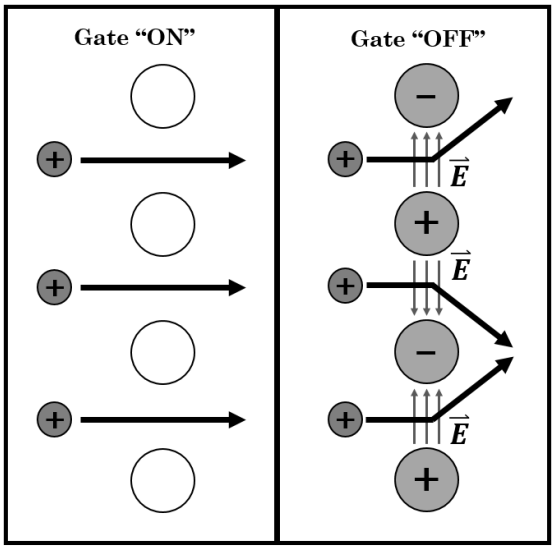

Fig. 3.1: Theory of Operation of BNG

Previous TOF-MS missions for space have used deflection gates with parallel plates instead of BNGs. Deflection gates use the same principle of operation, using two parallel plates to create perpendicular electric fields to deflect particles away from the instrument detector. Deflection gates are constructed from two metal plate electrodes on either side of the particle stream. Despite BNG gates being harder to fabricate, especially on the scale appropriate to CubeSats, they have several advantages over deflection gates with parallel plates. The electrodes of deflection gates can be up to several centimeters along the axis of the instrument. BNG electrodes, however, are extremely thin wires (several micrometers in diameter) arranged in a single plane perpendicular to the instrument axis, so in any design, the BNG will take up less axial space in the instrument than a deflection gate with parallel plates. The strength of an electric field is proportional to the voltage drop across electrodes and inversely proportional to the distance between electrodes. The fine spacing of the BNG electrodes yields a higher deflection field strength for a given potential drop than can be achieved by a gate with wider electrode spacing. The close proximity of the wires also helps contain the fringing of the electric field. While fringing effects are still present, they extend into other regions of the instrument in the same proportion as the electrode spacing, so fields created using finely spaced electrodes will contaminate less of the adjacent

sections of the instrument. The fine wires of the BNG have very little volume and would have very low capacitance when compared to larger electrodes. Although miniature BNGs are not commercially available for this project, there are published fabrication techniques for miniature BNGs that make it reasonable to include it in the instrument design.

3.3 Goals for Switching Voltage Driver Design

Goals for the performance of the BNG Driver design are based on a desire to improve upon the performance of a previously designed driver. The previous version was created at SDL to drive the miniature BNG gate for a linear TOF-MS instrument intended for use on a sounding rocket. This driver is capable of applying a 40 V drop across the sides of the gate and can create pulses as short as 70 ns FWHM with 20 ns of rise or fall time. The voltage output produced by this driver has the necessary characteristics to create well-defined packets from the sample stream because the response is smooth and flat at the common voltage level (the "ON" state of the gate) with little ringing. The goal for the new driver electronics was to create a voltage output of similar quality to the previous driver. The new driver is intended to create pulses significantly shorter than the previous version, in order to further reduce the mass resolution degradation caused by the gate open time. The minimum tolerable gate pulse width varies depending on many aspects of the instrument design, so the design goal is to simply reduce the 70 ns FWHM. The possibility of creating a driver which can apply higher voltage drops across the gate during the "OFF" state while still meeting the pulse width goals is considered a stretch goal for the driver.

The original design for the previous driver had a smaller pulse width of about 40 ns, with a filter added to the output in order to smooth out some significant ringing during both the "ON" and "OFF" phases of the gate. Avoiding ringing in the output of the driver is important because any difference in voltage between gate sides will result in deflection when the gate is open (the "ON" state). At a certain level, small deflections occurring during the "ON" phase of the gate would prevent some particles from hitting the detector, reducing the sensitivity of the instrument.

3.4 Driver Operation and Circuit Design

The driver circuit portion of the design consists of a Boost Supply MOSFET Driver chip, two MOSFET gates (a "top gate" and a "bottom gate"), a set of two differential logic level inputs, a chip power supply (V_{cc}), and a boost power supply (V_b). A diagram of the driver circuit is shown in Figure 3.2. Bypass capacitors and a diode are included per manufacturer's recommendations to help handle quickly switching voltages and high currents. The full design includes two driver circuits, one for the "low" side of the gate and one for the "high" side of the gate. The low side of the gate is biased at -75 V (the ground pin is tied to -75 V with the boost voltage tied to 0V) and the high side is biased at 0 V (the ground pin is tied to 0 V with the boost voltage tied to +75 V). The output, or "TS" pin, of each driver circuit is connected to one side of the BNG. The top gate ("TG" pin) and bottom gate ("BG" pin) are connected to the MOSFET gate inputs.

The driver works by changing the top and bottom gate inputs ("TINP"and "BINP") to either switch the top gate on (bottom gate off) to tie the output to the boost voltage or the bottom gate on (top gate off) to tie the output to the driver circuit ground. To turn the gate "ON", each driver is switched to the common voltage between the two sides. When the driver is "OFF", each output is pulled to the opposing voltage (+/- V_b volts away from the common voltage). This pattern is shown in the circuit simulation output in Section 3.4.2. The inputs for each driver circuit must be biased to the same voltage as the ground pin for that driver chip.

The signal timing for the "high" side of the gate driver is shown in Figure 3.3. Each element between the logic level control signal and the driver circuit introduces additional propagation delay between the command to open/close the gate and the gate actuation. This delay must be accounted for when calculating the particle mass from the arrival time.

The output load for this design is the BNG, with each side connected to one of the driver circuit outputs. Impedance measurements of the gate show that the load seen at the driver output would look like a small capacitive load of about 55 pF (see Table 3.1 for measurements). These measurements were used to design the circuit load for the simulation

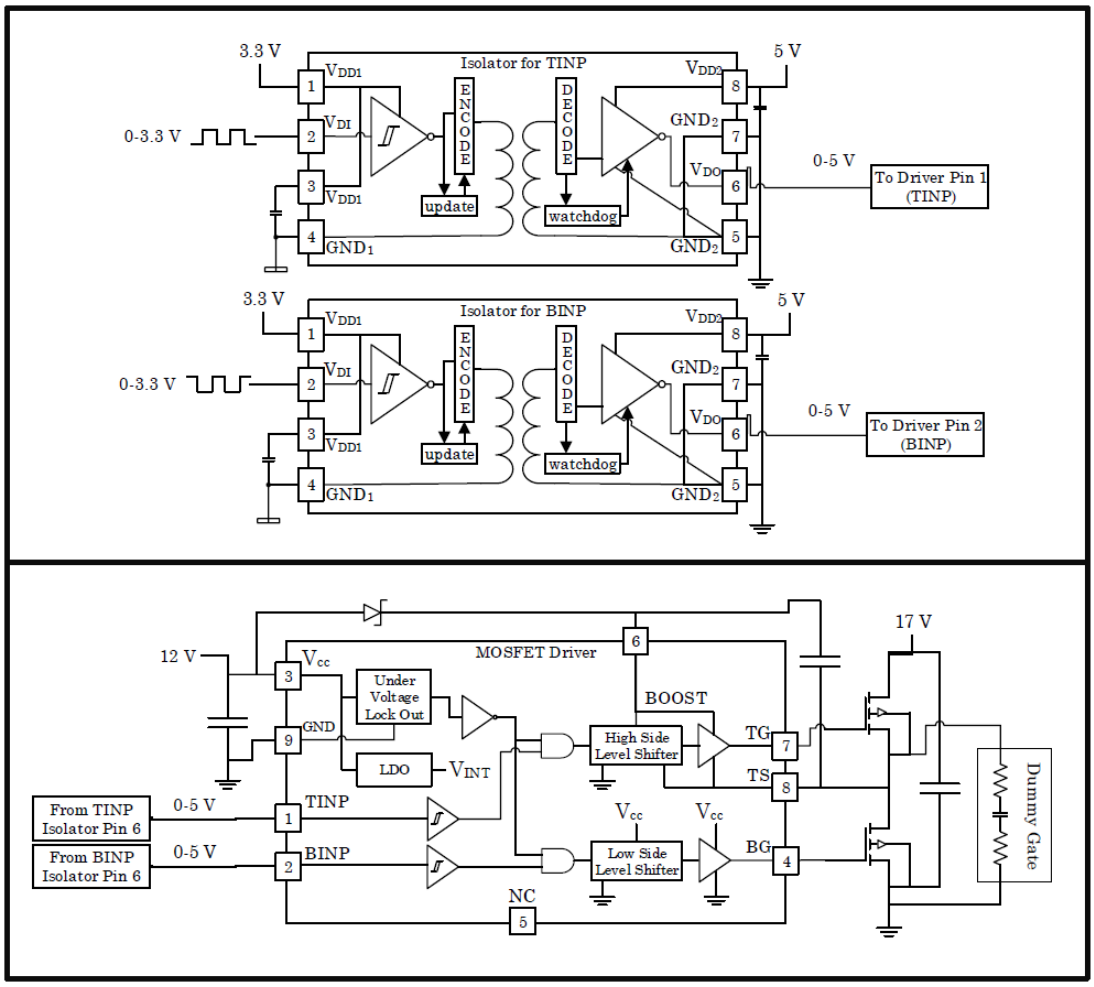

Fig. 3.2: Block Diagram of Driver Circuit

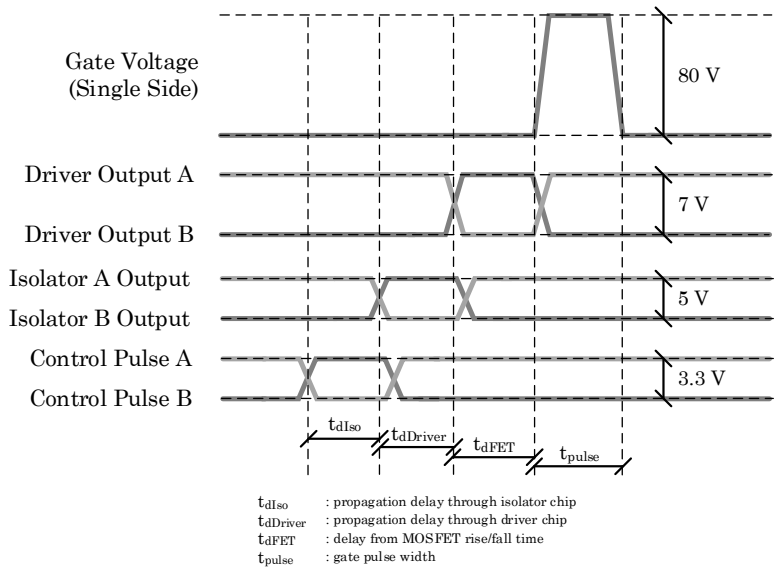

Fig. 3.3: Driver Timing Diagram ("High" Side Driver Circuit)

and the dummy load for testing the voltage driver.

3.4.1 Driver Circuit Components

Components from the previous driver design were used as a starting point for the new driver design. The previous design was created using logic level signals fed through comparators and amplifiers to increase the voltage level. The levels and timing achieved by the previous design were used as requirements when evaluating new components. Voltage limits and slew rates on newer amplifiers and comparators did not improve significantly upon the characteristics of the previous components. Therefore, designs that could be created from different types of components were considered for the new design, with the intent to surpass the voltage and timing limits of the comparators/amplifiers used for the previous design.

The MOSFET driver featured in the new driver circuit was designed to quickly switch outputs with a significantly higher voltage drop. The switching speed of the driver chip is limited by the propagation delay between receiving a differential, logic-level input and

Table 3.1: Table of Mini BNG Impedance Measurements

Test Frequency (Hz)	Test Amplitude (V)	Capacitance (pF)
50	1	55 - 56
100	1	55.6
1k	1	55.3
10k	1	55.2
100k	1	54.1

producing the output signals to control the MOSFET gates (25-27 ns). The maximum potential drop is the "boost" voltage limit (120 V above the ground pin input). The driver chip requires a differential, logic-level input and can be easily controlled by an FPGA or uController. The gate operation requires voltage switching from a common voltage level to an equal but opposite potential drop on either side. The chip can only switch between its ground pin input and the "boost voltage", but can operate at a biased ground level, so that two separate chips can switch each side of the gate to the common voltage and a higher or lower voltage. The driver inputs must be biased to the same potential as the ground pin input, so high-speed isolators are needed to shift the control signals. The driver chip is connected to two high-voltage, high-current tolerant MOSFETs. The rise/fall time of the driver output contributes to the overall pulse width of the driver circuit, so the MOSFETs were chosen for their fast rise/fall time (3 and 5 ns). A miniature high-voltage supply creates the high "boost" voltage, with buck regulators to supply power to the driver chips, isolators, and other components. The driver circuit (driver chip and MOSFETs) requires bypass capacitors and other peripheral components to achieve internal level shifting and provide a source for transient currents produced during the driver chip operation.

3.4.2 Simulation of Driver Circuit

Prior to construction and testing, the driver circuit was simulated in LTSpice. The simulation included two driver circuits (one for each side of the gate), ideal voltage sources, voltage buck regulators, ideal control signal inputs, and a lumped parameter model of the miniature BNG to simulate the output load. The simulation showed that the driver circuit can potentially produce a 27 ns pulse with rise/fall times of 3-5 ns. The possible voltage drop

across the sides of the gate was up to 200 V. The simulation did not show any significant ringing in the driver circuit output.

3.5 Driver Circuit Tests

3.5.1 Verification Board for Driver Circuit and Control Signals

The first prototype, the "verification board" was created to test the practical function of the driver circuit. This board contains only one side of the gate driver: one driver chip, one set of peripheral components, one pair of MOSFETs, and one pair of input isolators. Power is provided by laboratory voltage supplies through mounted connectors. The input control signals and output pin are also routed to mounted connectors. A separate "dummy gate" circuit was built, to connect to the driver output and represent the load created by the actual BNG. The other side of the dummy gate is tied to the driver circuit ground.

3.5.2 Driver Test Board for Full Design

A high-level layout of the test board for the BNG gate driver is shown in Figure 3.5. The test board contains a driver circuit for each side of the gate, isolators, a power supply, connections for the test loads, and a daughter board that will be used to control the drivers.

The driver circuits are as described in Section 3.4. Additional resistance and capacitance have been added to the inputs and outputs to help mitigate noise. The high side driver circuit ground is kept at the ground for the board, and the low side driver circuit ground is biased at -75 V and referred to as the floating ground.

A daughter board uController will be attached to the test board so that the driver pulses can be controlled from a PC. The daughter board will supply input signals and power one side of the isolators. The daughter board ground will be tied to the PC ground and isolated from the floating ground and test board ground.

An isolator circuit for each of the four inputs shifts the logic level from 3.3 V to 5 V. The isolator output ground pins for each driver circuit are tied to the ground pin of the driver circuit they are connected to and separated from the ground pins of the isolators

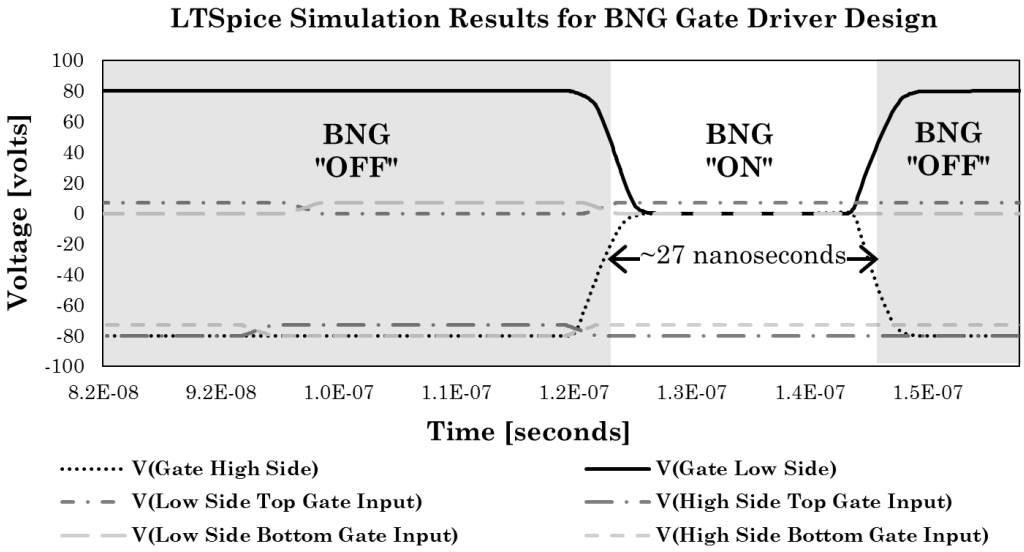

Fig. 3.4: BNG Driver Simulation Results

for the other driver circuit. In this configuration, the 5 V output of the isolators toggles between 0 and 5 V above the ground rail for the respective driver circuit.

The test board is capable of driving three different test loads: a dummy load (matching the lumped parameter model from the simulation), a spare miniature BNG mounted directly on the end of the board, and a BNG installed in a linear TOF-MS.

3.6 Testing and Troubleshooting

Testing of both the verification board and the test board revealed several aspects of the MOSFET driver implementation that will inform future revisions of the gate driver.

3.6.1 Driver Power Bypass Capacitance

The verification board tests revealed issues with the power bypassing that are critical to the driver operation. The verification board was originally built with a single bypass capacitor on the driver V_{cc} pin, sized according to the driver chip data sheet. Initial test data showed that, although the driver input signals had pulse widths of 25 ns, the driver output had much larger pulse widths, on the order of 1 us. The output pulse widths decreased when the current limit on the V_{cc} power supply was increased. It was theorized

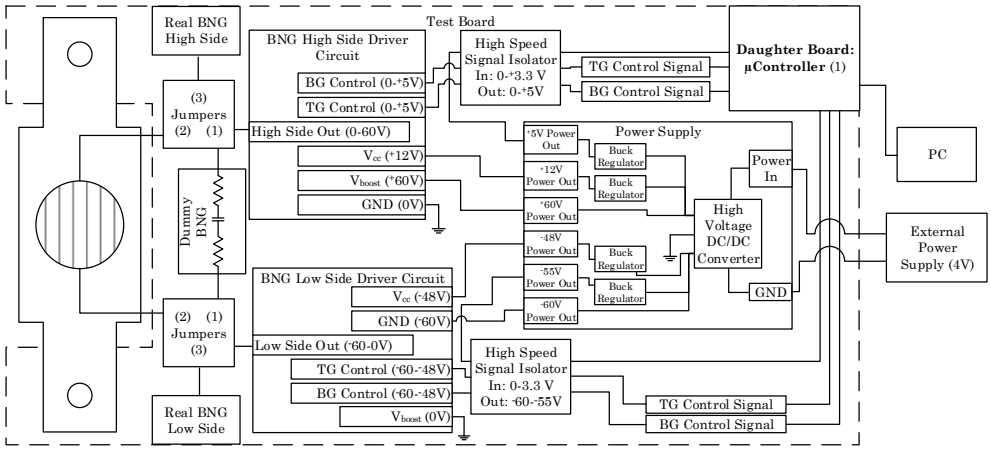

Fig. 3.5: Driver Test Board Layout

that the driver level shifters required a faster supply of transient current during switching to recharge enough to drive the high side MOSFET gate. The addition of several smaller bypass capacitors across the V_{cc} and ground rails resulted in driver output pulse widths that matched the input signals. Several values of additional bypass capacitor were added, all in the picofarad range. As more small bypass capacitors were added, the circuit was able to switch higher boost voltages. The verification board results showed that using a bank smaller bypass capacitors is critical to the operation of the driver.

3.7 Results

The driver circuit testing revealed that this design could potentially be an excellent solution for driving BNGs. Although the prototype printed circuit board (PCB) was not entirely functional, the driver circuit performs when biased to both Earth ground and a negative voltage, showing that the same circuit can be used to drive both sides of the gate. The test data shows the circuit switching a boost voltage of 30 V, which improves upon the voltage limit of the previous design (20 V drop for one side of the gate). In addition, the pulse widths of the output are approximately 35 ns, which also improves upon the previous design. Some ringing is present in the driver output, however, so further research is required to complete this design.

3.7.1 Negative Biasing the Driver Circuit

To verify the operation of the driver circuit at a negative ground bias, the high side circuit on the test board was supplied with boost voltage rails of Earth ground and +15 and -15 and Earth ground. The output of the driver with each of these biases is shown in Figure 3.6 and Figure 3.7.

Although the quality of the output signal is poor in both of these tests, the driver circuit successfully switches both up and down with both sets of voltage rails. This confirms that the driver can be used to operate both sides of the BNG despite the failure of the low side circuit on the test boards.

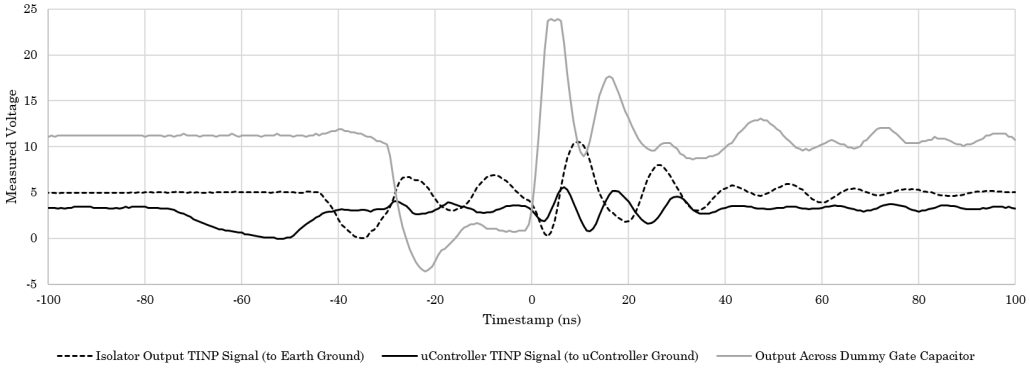

Fig. 3.6: High Side Driver Circuit with Driver Ground at Earth Ground
Note: The signal label names the placement of the high side of the oscilloscope probe and the parenthesized part of the signal label names the placement of the ground lead of the probe.

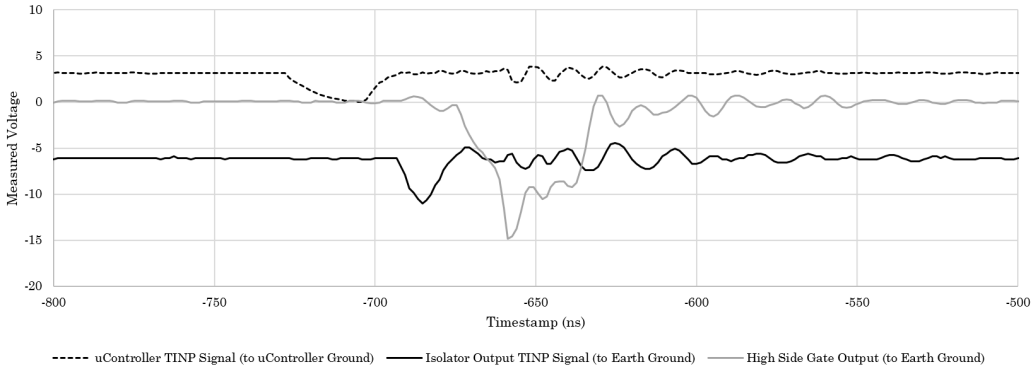

Fig. 3.7: High Side Driver Circuit Output with Driver Ground at -15V
Note: The signal label names the placement of the high side of the oscilloscope probe and the parenthesized part of the signal label names the placement of the ground lead of the probe.

3.7.2 Effect of Probe Impedance

The ringing present on the oscilloscope input during both verification and test board tests, if it were a product of the design operation and not the test setup, would mean that the driver output would not be suitable to drive a BNG. Additional testing was performed to determine if adjusting the impedance of the oscilloscope probes would eliminate or reduce this undesired noise. The output from tests of the high side driver circuit on the test board with a standard probe setup (using an alligator clip for the ground lead) is shown in Figure 3.8. The output from a test of the high side driver circuit on the same board with a short wire lead replacing the alligator clip is shown in Figure 3.9. Both tests were run with a regular probe setup for the uController input signal and the isolator output signal. Shortening the ground lead led to a reduction in the noise of the driver output. Another test, discussed in Section 3.7.3, showed that using probes with short ground leads on both the gate and the isolator output signals shows even less ringing in the driver output. This result suggests that the ringing can largely be attributed to the probe characteristics.

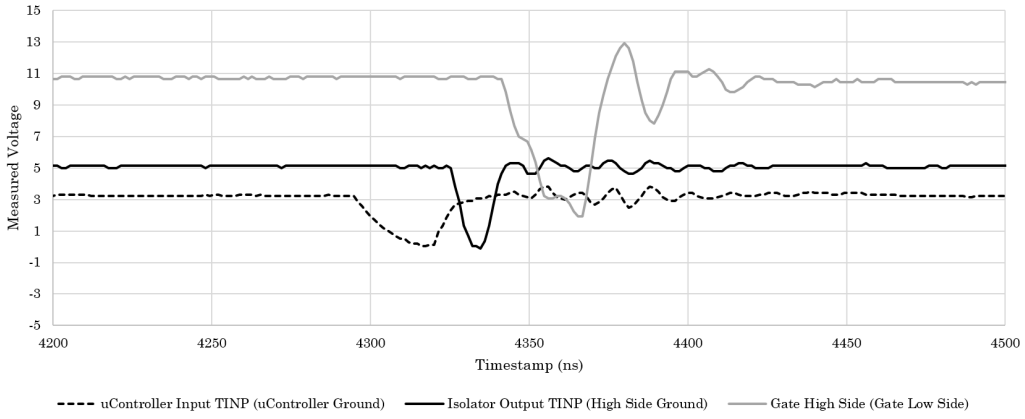

Fig. 3.8: High Side Driver Circuit Output Regular Probe Setup at Gate
The signal label names the placement of the high side of the oscilloscope probe and the parenthesized part of the signal label names the placement of the ground lead of the probe.

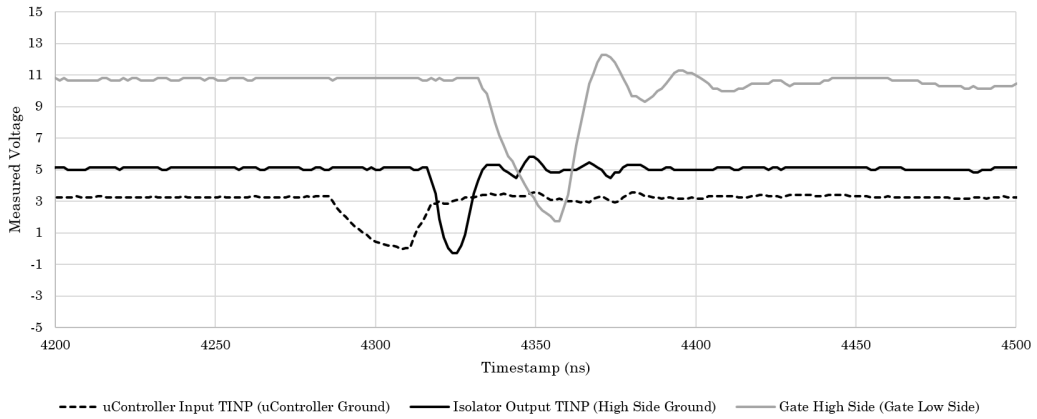

Fig. 3.9: High Side Driver Circuit Output with Low Inductance Ground Lead Probe at Gate

The signal label names the placement of the high side of the oscilloscope probe and the parenthesized part of the signal label names the placement of the ground lead of the probe.

3.7.3 High Voltage Test with Short Ground Leads on Probes

The previous driver design was capable of switching 40 V across the miniature BNG (+20 V and -20 V). Most testing of the new driver design was performed with a boost voltage drop of 15 V due to limitations from the bypass capacitance (on the verification board) and the bench-top power supplies. The test board design included a DC/DC converter capable of supplying up to 75 V of boost voltage drop for both sides of the circuit. However, this converter could not be used as installed to test the high side circuit without also powering the damaged low side circuit, so the converter was removed from the PCB. A test of the high side circuit was performed with the ground rail at earth ground and the boost voltage at 30 V. The results of this test are shown in Figure 3.10. This test setup used probes with short ground leads for both the isolator output and gate voltage signals. The result shows that the new driver design can exceed the voltage drop of the previous design.

In Figure 3.10, the voltage at the gate transitions with a slew rate of approximately 1 V/ns. This rise/fall time for this test is slower than that seen with shorter voltage drops. This is probably due to the resistor in the dummy gate load limiting the current flow to the capacitor representing the BNG. The slew rate for the driver output could be increased if the resistance between the gate driver output and the gate capacitance is minimized.

The resistor provides a filtering effect for the gate output in addition to representing the resistance in the gate wires and leads. Testing the driver on an actual BNG, which may have lower resistance than the dummy gate, would show if the slew rate of the gate output can be improved.

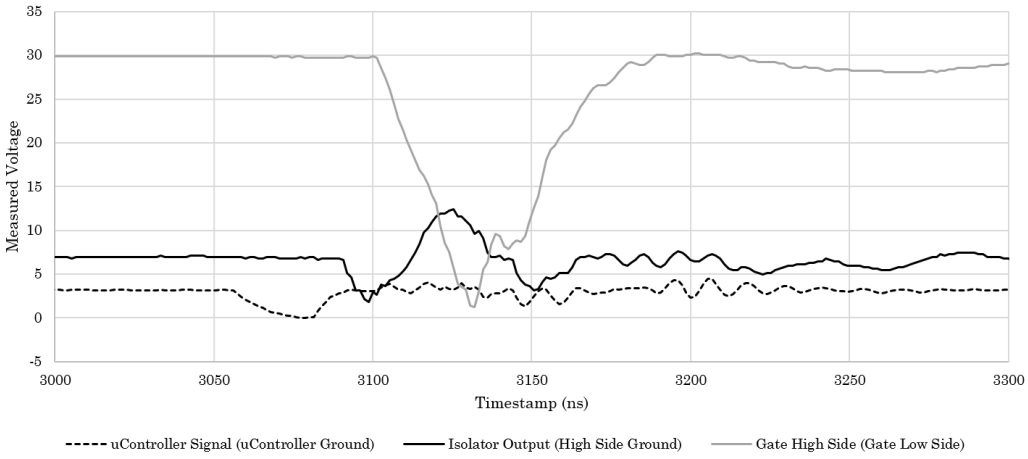

Fig. 3.10: High Side Driver Circuit Output with Short Ground Lead Probes on All High Side Signals

The signal label names the placement of the high side of the oscilloscope probe and the parenthesized part of the signal label names the placement of the ground lead of the probe. Both the isolator output signal and gate output signal are measured using probes with shortened ground leads.

Chapter 4

Detector Design

4.1 Instrument Detector System Design

The instrument detector will be used to measure the arrival times of particles at the end of their flight through the instrument. The design will use an MCP detector along with additional electronics to quantize and store the detector output. Measuring the number of particles is important for determining the composition ratios in a sample(s). Measuring the arrival times indicates which particle mass is being counted.

4.2 Design Considerations

The detector electronics design considers mainly the shape and form of the MCP output signal and the frequency of particle arrivals at the detector. For a single particle impact, the detector should produce a pulse that measures 750 ps FWHM at a voltage below logic level. However, the size, shape and duration of the detector output will change for multiple particle impacts, depending on the number of impacts and the spacing between them. To simplify, two types of particle impact sequences were considered. First, there is the case where few enough particles of each mass have entered the instrument that each particle impact will be distinctly separated in the detector output signal. In this case, the distance between particle arrivals will be greater than the pulse width of the detector, so each impact is counted separately and each pulse from the detector will have roughly the same amplitude and shape. Second is the case where enough particles of each mass have entered the instrument that arrival times will begin to bleed together. In this case, the distance between particle arrivals may be less than the detector pulse width, causing the detector output signal to change in amplitude and shape as each additional impact creates additional

output before the detector signal has recovered from a previous impact.

In the first case, the detector could simply identify when a pulse arrives and either count the total number of pulses or provide the arrival time of each pulse. Pulse detection can easily be achieved using a constant fraction discriminator (CFD). Using a CFD requires that the input pulses all have the same shape and so is well suited for identifying individual particle arrivals and provides highly accurate timing information. Pulse detection can also be achieved using thresholding. Simple thresholding uses comparators to identify pulses and does not provide timing information as accurately as CFDs. For the second case, it is expected that particle arrivals would be dense enough to cause the detector to output a pulse similar to the distribution curve of the particle arrivals. An analog-to-digital converter (ADC) could be used to measure the detector output and determine the height of the detector output.

Detector electronics designs for previous instruments have been built to cover either of these cases or both if two detector circuits are used together. This design will be built to measure a detector output from distinct, single particle impacts where arrival times are separated by more than the detector pulse width (i.e. the first case described in this section). This instrument is intended for use mainly in the thermosphere, where density will likely be low enough that the conditions on separated particle arrivals will be met. Several aspects of the instrument design could be adjusted so that the conditions will continue to hold even in the lower altitudes of the instrument's range.

4.3 Design Outline

A block diagram of the instrument signal is shown in Figure 4.1. The instrument signal begins when charged particles enter the instrument through the aperture. The instrument gate either deflects the particles (turning the signal off) or allows them to continue along the instrument axis (turning the signal on). The ion optics of the instrument then separate the particles by mass. Particles then hit the MCP detector, which converts the particle arrival into an analog signal (an asynchronous series of current pulses). Pulse detection electronics convert the detector signal to logic-level pulses. These pulses are counted by an

asynchronous ripple counter built within an un-clocked portion of a field programmable gate array (FPGA). The counter is periodically read and cleared to assign the particle counts to a particular bin. Another portion of the FPGA is clocked and used to control the gate driver, clear the counters, and process the count data for each bin.

4.4 Detector Device

Section 1.6 section describes MCP detectors, one type of particle detector that could be used in the detector system for this instrument. An MCP is an electron multiplier device, meaning that the device emits and collects a cascade of secondary electrons upon particle impact. There are other concepts for electron multiplier detectors that produce an output signal similar to an MCP but have different packaging that may be better suited to this instrument. One example of this is avalanche photodiodes, which have been tested as particle detectors and could be used as detectors for this instrument [15].

In short, an MCP or other electron multiplier device works by generating a pulse (small transient change in voltage) in the detector output signal when a charged particle of sufficient energy impacts the detector active area. The output pulse is expected to be very small in magnitude, around 1-2 mV, and must be amplified before it can be processed.

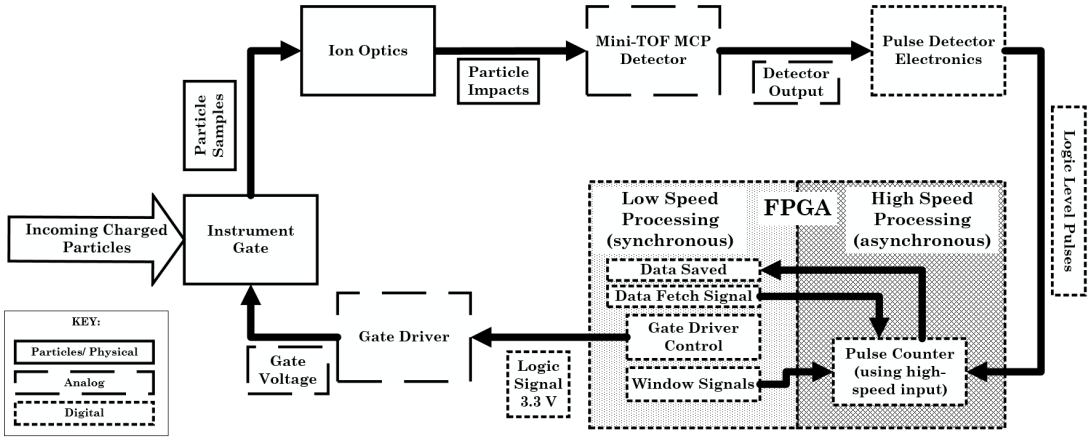

Fig. 4.1: Block Diagram of Detector System Design

4.5 Pulse Detection

The pulse detector electronics perform filtering, amplification, and thresholding to identify pulses in the detector output and convert them to logic-level signals. An outline of the pulse detector system is shown in Figure 4.2.

First, high-pass filtering can be used to remove the DC component of the detector output, which will have a high-voltage bias required for the MCP to operate. This stage of the pulse detector will need to have a bandwidth slightly lower than the signal frequency of 1 GHz to reject any DC bias but still allow particle arrival pulses through.

The signal amplitude is then amplified using a high-speed amplifier. The detector pulse is expected to have an amplitude of a few millivolts, so 100x amplification is needed to have a signal on the order of 1 V. This amplifier must have a bandwidth higher than the signal frequency and be capable of amplifying the signal without significantly widening the pulse widths. Therefore, the amplifier needs a bandwidth of 2.6 GHz or higher with a slew rate goal of 500 V/us.

The signal can then be further amplified. The second stage amplifier needs to have the same bandwidth as the first stage with slew rate increased to match the amplification (i.e. 2x the slew rate for 2x amplification). However, given that the FPGA input bandwidth is 900 Mbps, minimal stretching of the amplified signal could be allowed.

The amplified signal is then compared to a threshold value to separate particle impact signal from random noise. The comparator stage also converts the analog output into a

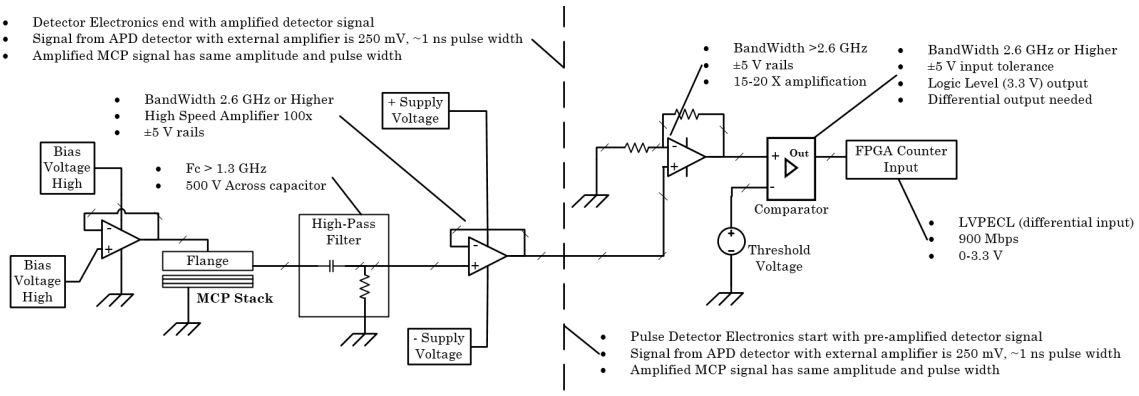

Fig. 4.2: Block Diagram of Pulse Detector Electronics

digital pulse that becomes the input to the FPGA counters. The comparator needs to output a 3.3 V differential signal to make it compatible with the high-speed low-voltage positive emitter coupled logic (LVPECL) input on the Igloo 2 FPGA that will be used to verify the detector system design.

4.6 FPGA Pulse Counting

Once the detector output has been converted to a logic level pulse train, the pulses will be fed to the high-speed input on an FPGA to be counted. Inside the FPGA, a portion of the fabric will remain un-clocked. Asynchronous ripple counters, built using the logic gates in the FPGA fabric) will receive and count the pulses. Another portion of the FPGA fabric will be clocked in the tens of MHz. This portion of the FPGA will create control and timing signals for the gate driver, ripple counter reset, and data fetching from the ripple counter.

4.7 FPGA Program Design

The FPGA programming for this detector system design will divide the device into a clocked (synchronous) portion and an un-clocked (asynchronous) portion. The program layout is shown in Figure 4.3. The program is described in Section 4.7.1 and Section 4.7.2.

4.7.1 Un-clocked FPGA Fabric

Two asynchronous ripple counters will be built in the un-clocked portion of the FPGA fabric. They will be activated by signals from the clocked portion of the FPGA, called the window signals. The window signals will alternate which counter is active. The ripple counter inputs ("data" in Figure 4.3) will come from the output of the pulse detector system described in Section 4.5. These signals will enter the FPGA via the high-speed LVPECL inputs and routed to the un-clocked portion of the fabric.

Taking a total count of pulses occurring during each window effectively bins the particle arrivals into the active time of the window. The number of hits per bin will be recorded, instead of the arrival times of each individual particle.

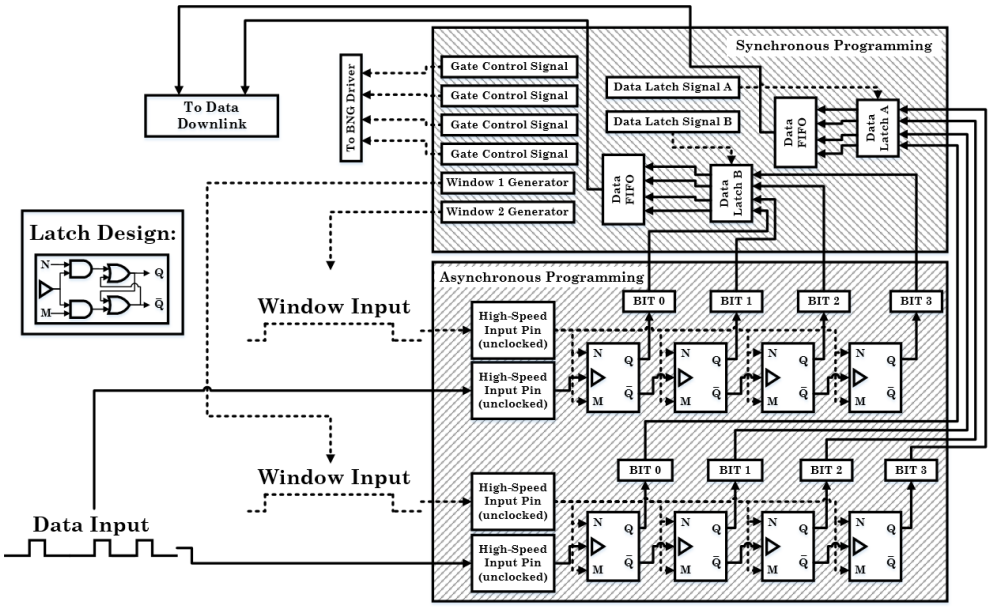

Fig. 4.3: Block Diagram of FPGA Program for Detector System

Figure 4.4 shows the window signals plotted with the estimated arrival time spectra for common atmosphere constituents. While this method can have a negative effect on the final mass resolution of the instrument, since the bins covering a single mass value will be wider than the arrival time distribution for that value, the instrument will still be able to distinguish between different constituents and determine the composition of the atmospheric sample. Since precision timing information, which could require multiple bytes of data for each particle, will not be saved, the volume of data the instrument produces will be significantly smaller. The number of hits per bin is likely to only require a single byte of data per bin, and the spectra could be compressed before downlink. Figure 4.4 has windows that are 100 ns in width (4 clock cycles on a 40 MHz clock). Adjustments to the width of the windows can be made to improve the performance of the instrument.

4.7.2 Clocked FPGA Fabric

Two window signals, two data fetch signals, and the gate driver control signals will be generated by the clocked portion of the FPGA fabric. The gate driver control outputs will act as “TINP” and “BINP” for the driver circuits (see Section 3.4).

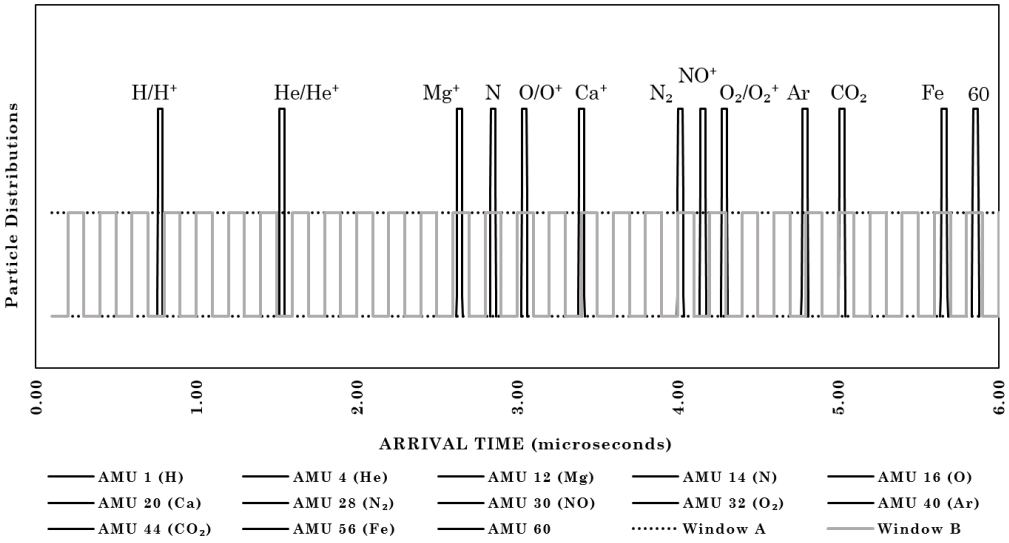

Fig. 4.4: Estimated Arrival Time Spectra with Detector System Windows

The window signals will activate and reset the ripple counters in the un-clocked fabric. There will be one window signal for each counter. While the window signal for a certain counter is high, any change in the input connected to that counter will change the counter bits. When the window is low, the bits will all be reset to zero.

The data fetch signals will be used to read the counter outputs and save them to memory. There will be one data fetch signal for each counter. When the data fetch signal goes high, the clocked portion of the FPGA will read the bit outputs on the counter and store them to memory.

The data fetch signal will latch the counter output so that any change to the bits after the latch signal will not be reflected in the data. Therefore, the time bin begins when the window signal for a counter goes high and ends when the data latch signal for the same counter goes high. The window signal for the next time bin will go high at the same time as the data latch for the previous time bin.

4.8 Design Verification Plan

Verifying the detector system design will require simulations, hardware testing, and full system testing with a dummy detector signal. The FPGA program has been simulated

in MATLAB (and will be converted to hardware description language (HDL) code to be tested on FPGA hardware as a future project). The pulse detector electronics will be simulated in Spice and then implemented in a prototype PCB. Then the output from the prototype pulse detector will be connected to the FPGA input to test the whole detector signal system. Input to the pulse detector system can come from a detector that produces 2.5 mV pulses with approximately 1 ns pulse width, or from a high-speed pulse generator capable of simulating the detector output.

4.8.1 Simulation Results

The proposed detector system FPGA program was simulated using MATLAB Simulink. The simulation consists of control signal generator blocks (where the Window, Data Latch, and Gate Control signals are generated), data latch blocks (where the bits of the simulated counter output are concatenated and saved), and data simulation blocks (where each bit of the counter output is simulated using a Bernoulli Binary random generator).

The control signal generator block is shown in Figure 4.5. The program uses one counter to generate the gate control signals and restart the measurement cycle and another to generate the window and data latch signals. Each signal is generated using a comparator or pair of comparators to switch the signal on and off. There are several adjustable values in the simulation: W is the number of clock half-cycles per window; GP is the number of clock cycles in the gate control signals; T is half the FPGA clock period in nanoseconds; C is the measurement cycle length in nanoseconds; and M is the amount of time, in nanoseconds, the start of the window and data latch signals are delayed.

The control signal generator output is shown in Figure 4.6. The output shows that the program can create the necessary control signals to fire the gate, activate the counters, and obtain data.

The data latch block is shown in Figure 4.7. In this block, the bits of simulated counter output are concatenated into a one byte data point. These data points are then stored in a data First-In-First-Out (FIFO) stack while they wait to be sent to the spacecraft bus for downlink. In this simulation, data is pulled back out of the FIFO when the next data point

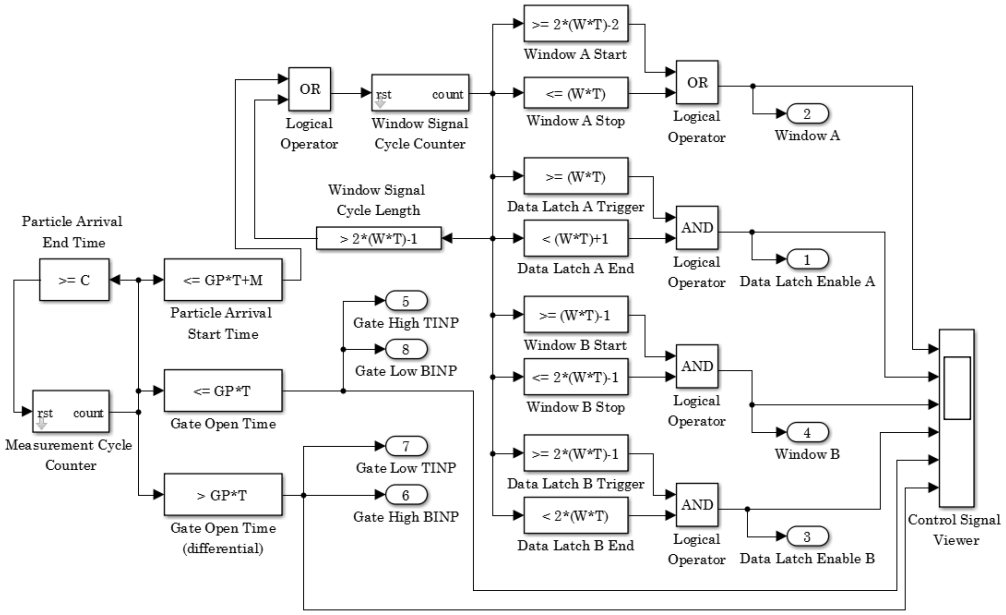

Fig. 4.5: Simulink Simulation of the Detector System FPGA Control Signal Generation

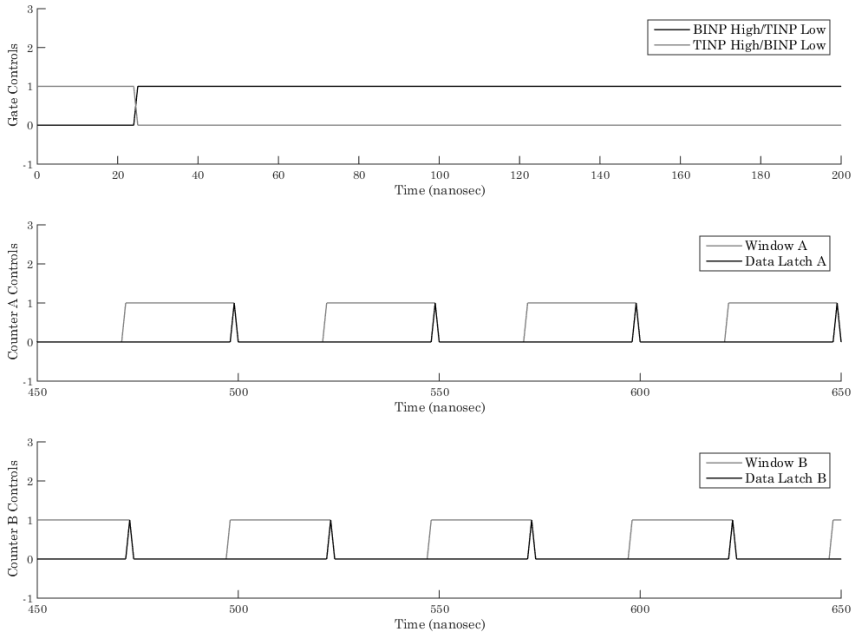

Fig. 4.6: Simulated Control Signal Generator Output

is saved. When implemented, more data points could be stored in the FIFO, with a separate program block responsible for pulling them from the FIFO and writing them to memory. The data output from this block is shown in Figure 4.8 along with the corresponding window and data latch signals.

A data simulation block was used to provide data for the program simulation. This block uses random Boolean generators to simulate each bit of a ripple counter for the data latch block to read. In implementation, a pulse generator would be used to create a one dimensional input signal that would be fed to a ripple counter. The ripple counter is not part of the synchronous FPGA program and the behavior is well known, so it was not included in the program simulation.

4.9 Discussion

4.9.1 Effect on Instrument Sensitivity

This detector system design assumes that the densities of samples are low enough that particle arrivals can be reasonably expected to occur far enough apart that there is no significant overlap of the signal output pulses. This places a limit on the number of particles of one species in one sample that the instrument can be expected to detect. As discussed in Chapter 2 Section 2.1.2, a limit of one pulse per 2 ns is used to factor this design effect into the instrument measurement range calculation.

4.9.2 Effect on Mass Resolution

As discussed in Chapter 2, the mass resolution of the instrument is calculated based on the mean arrival time and the width of the arrival time distribution. The smaller the arrival time distribution width, the higher the mass resolution. In this detector system design, precise timing information is not collected for each particle arrival, so the mass resolution would have to be calculated using the width of the window in which a constituent would arrive. The windowing of the mass spectra in this detector system is based on the synchronous clock. The windows it creates may not align perfectly with the arrival

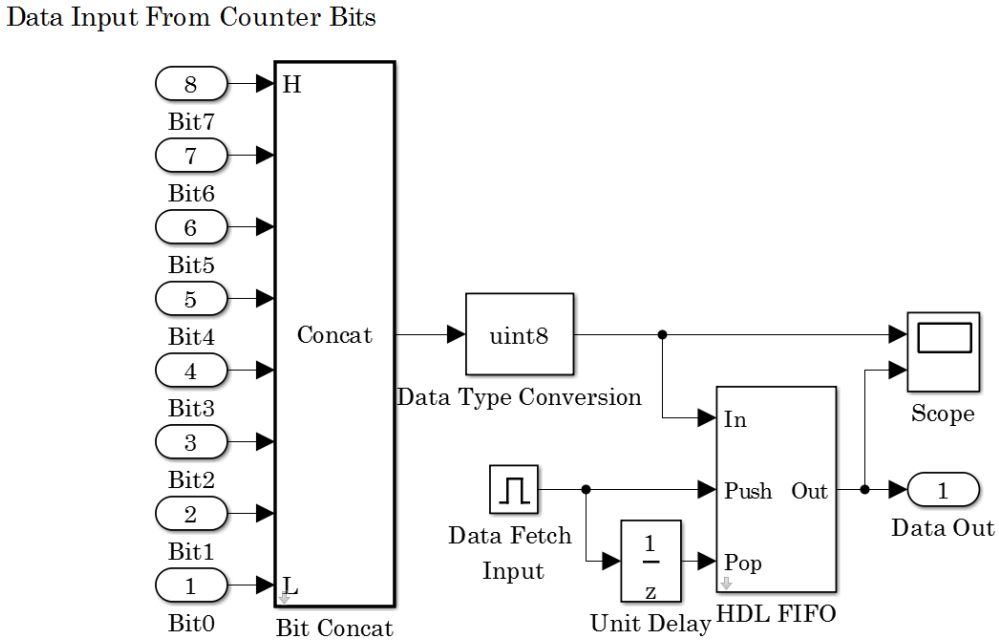

Fig. 4.7: Simulink Simulation of the Detector System Data Latch Block

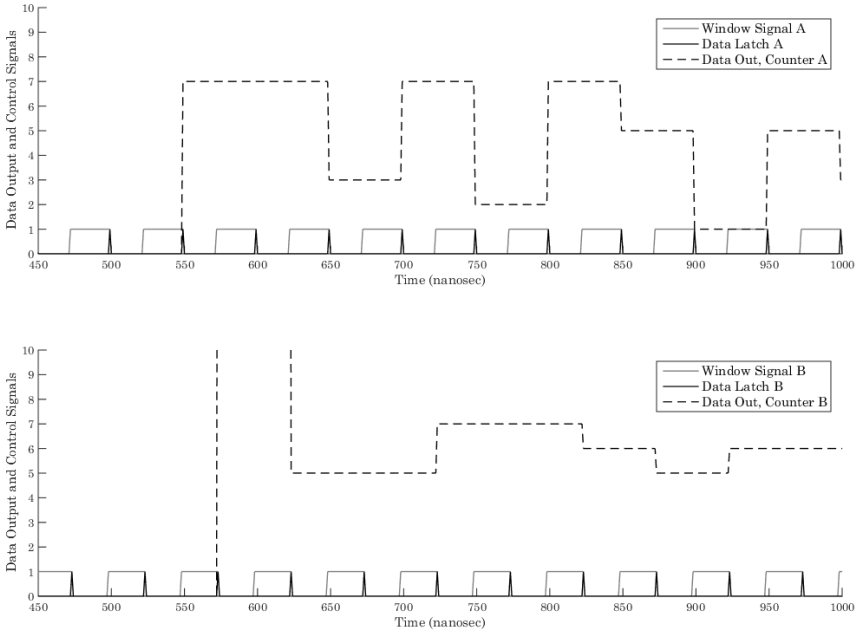

Fig. 4.8: Simulated Data Output from FPGA Program

time distributions for every constituent, or the windows may be smaller than the arrival time distribution. In some cases, two or more windows may be needed to cover a single constituent. Since the exact arrival times are not collected, the mass resolution for those cases would have to be calculated based on the width of all the windows combined. This mass resolution would be lower than that achieved by the instrument optics. However, the windows will be designed such that no window overlaps more than one constituent so that the instrument output still accurately represents the atmospheric composition despite the degradation in mass resolution.

Chapter 5

Instrument Completion and Integration

This thesis project has included a high-level instrument design, a feasibility analysis of that design, and the development of a BNG voltage driver and detector signal collector design to make the design possible. This chapter presents a plan to complete a functional prototype of the instrument that is appropriate to the organization and work structure at USU. This plan is designed with the assumption that graduate students will take responsibility for the projects and collaborate with research centers, such as SDL, that can provide access to facilities and expertise to make the design successful.

5.1 Summary of Instrument Design

This section summarizes design of the instrument thus far, which will define the requirements and constraints for small projects to develop the instrument. Table 5.1 shows the dimensions of the instrument, including axial dimensions of each component, the general width of the instrument, and the volume available for the instrument electronics.

Table 5.1: Instrument Dimensions

Component	**Axial Length**
Ionizer and Aperture	15 mm
MCP Detector	30 mm
Reflectron	45 mm
Flight Tube 1	21.31 mm
Flight Tube 2	10.6 mm
Accelerator Spacing (including gate thickness)	3 mm
Dimension	**Value**
Reflectron Angle	0.19 radians
Mounting Allowance	5 mm each side
Width of Electrodes	30 mm
Volume for Electronics	90 mm x 90 mm x 10 mm

Table 5.2 outlines the mass of the instrument by defining what percentage of the overall instrument mass should be allocated to each component or subsystem.

Table 5.3 outlines the power consumption of the instrument by defining what percentage of the overall instrument average power should be allocated to each component or subsystem.

Table 5.2: Instrument Mass Breakdown

Component	**Percentage of Total Mass**	**Mass Allowance**
Electronics	25%	250 g
Ionizer and Aperture	10%	100 g
Detector	5%	50 g
Flight Tubes and Reflectron Electrodes	38 %	375 g
Acceleration and BNG Grids	13%	125 g
Mounting Hardware	5%	50 g
Reserve	5%	50 g
Total		**1000 g**

Table 5.3: Instrument Average Power Breakdown

Component	**Percentage of Total Power**	**Power Allowance (Ion Measurement)**
Total Power		**2000 mW**
Ionizer	0%	0 mW
Electrode Drivers	26%	520 mW
Pulse Detector System	19%	380 mW
BNG Driver	26%	520 mW
Instrument Control and Pulse Counter	24%	480 mW
Reserve	5%	100 mW
Component	**Percentage of Total Power**	**Power Allowance (Neutral Measurement)**
Total Power		**2800 mW**
Ionizer	26.8%	750 mW
Electrode Drivers	18.6%	520 mW
Pulse Detector System	13.6%	380 mW
BNG Driver	18.6%	520 mW
Instrument Control and Pulse Counter	17.1%	480 mW
Reserve	5.4%	100 mW

5.2 Small Projects to Finish Subsystem Development

Remaining work on the instrument prototype has been divided into small projects to be done by graduate students within 1-2 years. These projects include electrical and mechanical design for the instrument electrodes, fabrication of the instrument acceleration and BNG grids, implementation of the detector system design, and the integration and test of the instrument. The current instrument design will impose requirements and constraints on each of these projects.

5.2.1 Instrument Electrode Design

The instrument electrode design includes the mechanical design and procurement of the instrument electrodes which will be used to create the electric fields within the instrument and shape the ion optics. The design shall determine the materials, construction, and shape of the containers for the field-free drift tube and reflectron of the instrument. The shape of the containers will be designed such that the samples that enter the instrument are contained and the field-free and reflectron regions can be isolated from each other via wire grids. The reflectron container shall be a grid-less reflectron. The number of electrodes and electrode spacing shall be chosen so that they can be used to create a quadratic-shaped retarding field.

The electrode design is subject to constraints imposed by the instrument requirements. The flight tubes and reflectron must be designed so that the instrument will fit within the $\frac{1}{2}$ U volume and shall require no more than 38% of the total instrument system mass. The requirements for the instrument electrode design are listed in Table 5.4.

Table 5.4: Instrument Electrode Requirements

Electrodes shall be made from materials on the NASA low-outgassing materials list.
The instrument electrodes shall be made from conductive material.
The non-electrodes of the instrument shall be made from non-conductive material.
The total mass of the electrodes shall not exceed 375 g.
Drift Tube 1 shall be 21.31 mm in length.
Drift Tube 2 shall be 10.6 mm in length.
The reflectron depth will be 45 mm.

The electrode design concept is based on the axial lengths from dimension optimization. The reflectron field shape is based on the preliminary analysis of particle trajectories in SIMION for several different field shapes. These analyses are discussed in Chapter 2. Before fabricating the electrodes, the full instrument design should be simulated in SIMION using the actual drift tube and reflectron electrode designs. The particle definitions for this SIMION simulation should include the full Maxwell-Boltzmann distribution of initial velocities in all three directions.

5.2.2 Instrument Grid Design

The instrument grid design includes the mechanical design and procurement of the wire grids that will be used to isolate different regions of the instrument ion optics. The design shall determine the materials, construction, and interface for the wire grids in several places on the instrument, including plasma and electron rejection grids (outside the aperture), the grid between the ionization and acceleration region, the BNG, the reflectron region entrance (end of the first drift region) and exit (beginning of the second drift region), and between the second drift tube and the detector (to create the final acceleration region). The grids shall be designed such that they do not significantly degrade the mass resolution or sensitivity of the instrument.

The grid design is subject to constraints imposed by the instrument requirements. The grid and any mounting equipment required must be designed so that the instrument will fit within the $\frac{1}{2}$ U volume and all of the grids combined shall require no more than 13% of the total instrument system mass. The BNG grid is subject to the additional constraint that the wires need to be nearly parallel.

The requirements for the instrument electrode design are listed in Table 5.5.

Table 5.5: Instrument Grid Requirements

The instrument grid frame shall not be wider than the instrument electrodes.
The grid frames shall be designed so that a 3mm spacing between grids can be achieved.
The fringing effects on electric fields adjacent to the grid shall extend no more than 5% into adjacent regions.
Each grid shall have a transmission efficiency of greater than 70%.

The grid design concept is based on designs used in several different types of particle detector instruments, including TOF-MS. The design will need to identify the dimensions of the grid mounting, the wire diameter, the wire material, and width of space left between the wires (where particles will pass through the gate). Published techniques (such as those published by Zare et al. [16]) can be used for this design.

5.2.3 Voltage Driver for Electrodes

The electrode voltage driver design includes the electrical design of a device to apply electric potentials to the electrodes of the instrument. The electrode voltages will control the ion optics of the instrument and have a significant effect on the mass resolution and sensitivity. The electrode voltage driver needs to apply voltage such that the instrument performs as closely as possible to design simulations.

The electrode voltage driver is subject to constraints imposed by the instrument level requirements. The electronics hardware needs to fit, along with all other instrument electronics, in the $\frac{1}{2}$ U volume allowed for the instrument electronics. The instrument electronics can require no more than 25% total of the mass of the instrument system. The electrode voltage driver can use no more than 26% of the total instrument power during ion measurement and no more than 18.6% of the total instrument power during neutral measurement.

The requirements for the instrument electrode voltage driver are listed in Table 5.6. The electrode voltage driver will need to apply high voltages, up to 5 kV. The device should consist of a single circuit board or portion of a circuit board with outputs for each required voltage level.

Table 5.6: Electrode Voltage Driver Requirements

The electrode voltage driver shall fit within the volume allowed for instrument electronics.
The instrument electronics shall require no more than 250 g.
The electrode voltage driver shall consume no more than 520 mW average power.

5.2.4 Implementing the Detector System Design

The detector system design implementation project requires the procurement of hardware and development of software to implement the detector signal collector described in Chapter 4. The software will be developed from a MATLAB simulation of the FPGA program design. The hardware shall be developed according to the requirements discussed in 4.5. The entire system shall be tested as discussed in 4.8.

5.3 Instrument Integration and Test

The instrument integration and test project is to assemble and interface the electrical and mechanical aspects of the instrument and characterize the instrument performance. The electrical and mechanical aspects of each portion of the instrument need to be integrated and each piece tested to ensure it meets requirements before the entire instrument is put together. Mechanical integration of the instrument will require designing the mechanical interfaces between each piece of the instrument, assembling the instrument, and designing mounting hardware. The detector signal collector and voltage driver electronics will be developed separately and then integrated into a single electronics package for the instrument, which will include an instrument control board. Once completed, the prototype instrument will need to be tested on a laboratory sample to determine the actual mass resolution and sensitivity performance. These tests would be compared to the instrument requirements described in Chapter 1 and the performance of the simulated instrument.

References

[1] J. L. Wiza, "Microchannel Plate Detectors," *Reprint from Nuclear Instruments and Methods*, vol. 162, pp. 587–601, 1979.

[2] J. M. Picone, A. E. Hedin, D. P. Drob, and A. C. Aikin, "NRLMSISE-00 Empirical Model of the Atmosphere: Statistical Comparisons and Scientific Issues," *Journal of Geophysical Research*, vol. 107, no. A12, p. 1468, 2002.

[3] E. M. Gaposchkin and A. J. Coster, "Analysis of Satellite Drag," *The Lincoln Laboratory Journal*, vol. 1, no. 2, pp. 203–224, 1988.

[4] M. Guilhaus, "Principles and Instrumentation in Time-of-Flight Mass Spectrometry Physical and Instrumental Concepts," *Journal of Mass Spectrometry*, vol. 30, pp. 1519–1532, 1995.

[5] R. P. Schmid and C. Weickhardt, "Designing Reflectron Time-of-Flight Mass Spectrometers with and without Grids: a Direct Comparison," *International Journal of Mass Spectrometry*, vol. 206, pp. 181–190, 2001.

[6] T. T. King, S. A. Getty, P. A. Roman, F. A. Herrero, H. H. Jones, D. M. Kahle, B. Lynch, G. Suárez, W. B. Brinkerhoff, and P. R. Mahaffy, "Simulation of a Miniature, Low-Power Time-of-Flight Mass Spectrometer for In Situ Analysis of Planetary Atmospheres," vol. 6959, no. 69590E, pp. 1–15, 2008.

[7] D. Ioanoviciu, "Ion-Optical Properties of Time-of-Flight Mass Spectrometers," *International Journal of Mass Spectrometry*, vol. 206, pp. 211–229, 2001.

[8] W. Wiley and I. McLaren, "Time-of-Flight Mass Spectrometer with Improved Resolution," *The Review of Scientific Instruments*, vol. 26, no. 12, pp. 1150–1157, December 1955.

[9] G. Scoles, Ed., *Atomic and Molecular Beam Methods, Volume 1.* New York, New York: Oxford University Press, 1988.

[10] M. Yildirim, O. Sise, M. Dogan, and H. S. Kilic, "Designing Multi-Field Linear Time-of-Flight Mass Spectrometers with Higher-Order Space Focusing," *International Journal of Mass Spectrometry*, vol. 291, pp. 1–12, 2010.

[11] D. Manura, *SIMION 8.0/8.1 User Manual, Revision 5.* Scientific Instrument Services, Inc.

[12] N. E. Bradbury and R. A. Nielsen, "Absolute Values of the Electron Mobility in Hydrogen," *Physical Review*, vol. 49, no. 5, pp. 388–393, 1936.

[13] E. A. Everett and E. Syrstad, "A Rocket-Borne Axially Sampling Time–of–Flight Mass Spectrometer for Investigation of the Upper Atmosphere," Poster, 2005.

[14] J. Oberheide, P. Wilhelms, and M. Zimmer, "New Results on the Absolute Ion Detection Efficiencies of a Microchannel Plate," *Measurement Science and Technology*, vol. 8, pp. 351–354, 1997.

[15] K. Ogasawara, S. A. Livi, M. I. Desai, R. W. Ebert, D. J. McComas, and B. C. Walther, "Avalanche Photodiode Based Time–of–Flight Mass Spectrometry," *Review of Scientific Instruments*, vol. 86, no. 8, 2015.

[16] J. R. Kimmel, F. Engelke, and R. N. Zare, "Novel Method for the Production of Finely Spaced Bradbury-Nielson Gates," *Review of Scientific Instruments*, vol. 72, no. 12, pp. 4354–4357, 2001.

Appendix

List of Included Files

A.1 Flight Time Estimation

Flight Time Estimation Tool

This spreadsheet is the final version of flight time estimation tool spreadsheet. It contains sheets for the instrument dimension fitting ("Dimension Calculator"), the flight time calculations ("Flight Times by Parts"), a plot for the FTET output through 60 AMU ("Flight Times AMU 60"), and a plot for the FTET output through 250 AMU ("Flight Times AMU 250"). "Flight Times by Parts" includes Macros for recalculating the estimated arrival time distributions after the instrument design has changed. It also includes a Macro for a preliminary dimension optimization study, and a section to calculate and plot the window bins that would be generated by the detector system.

Dimensions Diagram

This is an outline drawing of the instrument layout, including labels for the dimension variables used in FTET and dimension optimization.

Instrument Sections Block Diagram

This is a drawing to point out the basic regions of the instrument. It helps show how the FTET calculations are divided up.

Reflectron Field

This is a drawing to demonstrate the variables used to calculate the electric field in the reflectron.

Dimension Calculations

This is a set of equations for fitting the instrument inside the instrument volume.

TOF for Three Accelerators

This is a set of equations for the total time-of-flight calculation for an instrument with three acceleration regions.

TOF for One Accelerator

This is a set of equations for the total time-of-flight calculation for an instrument with one acceleration region.

Reflectron Field

This is a set of equations for the electric field calculation for the reflectron region.

Flight Time for Acceleration Region

This is a set of equations for calculating the particle flight time through a single acceleration region.

Flight Time for Reflectron

This is a set of equations for calculating the particle flight time through the reflectron region.

Flight Time for Drift Region

This is a set of equations for calculating the particle flight time through a field-free drift region.

A.2 Instrument Sensitivity Estimation

Measurable Density Estimation Tool

This spreadsheet is the final version of the Measurable Density Estimation Tool. It contains calculations to estimate the range of densities an instrument design will be able to measure. The inputs are values corresponding to parts of the instrument design which will affect the sensitivity of the instrument. The file uses ionization cross sections from an online data base and compares the instrument measurement range to density values from the MSIS and IRI models.

Sensitivity Calculation

This is a set of equations for calculating for the sensitivity of the instrument to neutral particles.

Minimum Maximum Measurable Density Calculation

This is a set of equations for calculating the density measurement range for the instrument.

A.3 SIMION Trajectory Analysis

Trajectory Evaluation Results

This file contains details of the trajectory evaluation simulations and snapshots of the resulting trajectories from the two non-linear fields tested.

A.4 SIMION Compared to FTET

SIMION and FTET Data

This file contains flight times and plots from various SIMION simulations and FTET results run using the same instrument designs to compare the two tools.

SIMION to Verify FTET

This file contains details about the parameters of the SIMION simulations run to compare to the FTET results for certain instrument designs.

A.5 Dimension Optimization with Three Acceleration Regions

MATLAB File: "tof_calc.m"

This code calculates the estimated arrival time of a particle given the instrument dimensions, voltages, and particle initial conditions.

MATLAB File: "tof_dimensions.m"

This code calculates the length of the drift regions given the accelerator spacing and reflectron depth.

MATLAB File: "tof_mass_res.m"

This code calculates the mass resolution for a design by using "tof_calc.m" to the arrival time for 60 AMU with mean initial velocity, mean initial velocity plus the thermal velocity, and mean initial velocity minus the thermal velocity.

MATLAB File: "tof_search.m"

This code searches for the optimal design by using "tof_dimensions.m" to find neighboring designs, then uses "tof_mass_res.m" and "tof_calc.m" to find the performance of each of the neighboring designs. Repeats until local maxima is found.

A.6 Dimension Optimization with One Acceleration Region

MATLAB File: "tof_calc.m"

This code calculates the estimated arrival time of a particle given the instrument dimensions, voltages, and particle initial conditions.

MATLAB File: "tof_dimensions.m"

This code calculates the length of the drift regions given the accelerator spacing and reflectron depth.

MATLAB File: "tof_mass_res.m"

This code calculates the mass resolution for a design by using "tof_calc.m" to the arrival time for 60 AMU with mean initial velocity, mean initial velocity plus the thermal velocity, and mean initial velocity minus the thermal velocity.

MATLAB File: "tof_search.m"

This code searches for the optimal design by using "tof_dimensions.m" to find neighboring designs, then uses "tof_mass_res.m" and "tof_calc.m" to find the performance of each of the neighboring designs. Repeats until local maxima is found.

MATLAB Published Results: "tof_calc.m"

This file is the MATLAB publisher output for the version of this code used for the dimension optimization for a single accelerator design.

MATLAB Published Results: "tof_dimensions.m"

This file is the MATLAB publisher output for the version of this code used for the dimension optimization for a single accelerator design.

MATLAB Published Results: "tof_mass_res.m"

This file is the MATLAB publisher output for the version of this code used for the dimension optimization for a single accelerator design.

MATLAB Published Results: "tof_search.m"

This file is the MATLAB publisher output for the version of this code used for the dimension optimization for a single accelerator design. This file contains the optimized

design parameters.

A.7 Full Instrument CAD Model

Design Layout Assembly

This is a assembled model of all the instrument parts.

Part File: Detector

This is a model of the MCP detector, provided by Photonis. "detector_product.par"

Part File: Drift Tube One

This is an electrode model for the first drift tube. "55mm_design_flight_tube1.par"

Part File: Drift Tube Two

This is an electrode model for the second drift tube. "55mm_design_flight_tube2.par"

Part File: Aperture

This is a model of the aperture for the design layout assembly. "aperture.par"

Part File: Ionizer Box

The is a model of space required for ionizer for design layout assembly. "ionizer.par"

Part File: Gate and Accelerator

These are electrode models for the fine accelerator and BNG grids. BNG model does not have gating function. "square_accel_grid.par" and "square_bng_grid.par"

Part File: Reflectron Assembly

This is an electrode model assembly for the 55 mm reflectron. Separate rings assembled into one piece. "55mm_Reflectron_Assembly.asm". Ring part files included in sub-folders.

Part File: Angled Reflectron Assembly

This is an electrode model of the reflectron assembly, with the reflectron shape angled so that proximity to the reflectron wall is the same for particles coming in and going out. "Angled_55mm_Reflectron_Assembly.asm" Ring part files included in subfolders.

Part File: CubeSat XY

This is a model of walls of a 1U CubeSat. This is used to create design layout assemblies.

Part File: CubeSat Z

This is a model of the posts with the top and bottom surfaces of a 1U CubeSat. This is used to create design layout assemblies.

A.8 Instrument Requirements List

This spreadsheet lists the instrument level requirements. It includes breakdown tables for instrument mass and power.

A.9 Instrument Gate

BNG Explained

This is a drawing to demonstrate how the BNG works.

A.10 Instrument Gate Voltage Driver

Driver Circuit Block Diagram

This is a simplified schematic of the gate driver circuit for just one side of the gate.

Driver Circuit Timing Diagram

This is a drawing to show the propagation delays between the control signal at the isolator input to the driver circuit output.

Driver Chip Datasheet

This is the datasheet for the MOSFET driver chip, LTC4446.

MOSFET Datasheet

This is the datasheet for the MOSFETS, FDMS86104.

Diode Datasheet

This is the datasheet for the diode, BAS21.

Signal Isolator Datasheet

This is the datasheet for the high-speed signal isolators, ADUM1100BRZ.

Buck Regulators Datasheet

This is the datasheet for the buck regulators, LTC3012.

High Voltage DC/DC Converter Datasheet

This is the datasheet for the EMCO High Voltage DC/DC Converter.

Spice Simulation: Two Driver Circuits with V_{cc} Buck Regulators

This is an LTSpice schematic which models two driver circuits (one for each side of the gate) powered from buck regulators and ideal high voltage sources. The circuits are connected via the dummy gate circuit.

LTSpice Driver Circuit Simulation Results

This spreadsheet contains the Spice simulation results for the gate driver.

A.11 Gate Voltage Driver Verification Board

Verification Board Outline

This is a drawing to explain the circuit on the verification board.

Driver Circuit Alone (Schematic and PCB Layout)

These files contain the schematic and PCB layout for the verification board (ordered through PCB Express).

A.12 Gate Voltage Driver Prototype Test Board

Test Board Test Plan Diagram

This is a drawing to explain the various test loads planned for the prototype test board.

Driver Test Board Block Diagram

This is a drawing to explain the electronics included on the driver test board.

Test Board Schematics

This folder contains the Cadence schematic files for the test board.

BNG Driver Test Board PCB Layout

This is a PDF print of the four layers of the test board PCB. Layers two and three are shown in negative polarity (white space is copper). Layers one and four are shown with regular polarity (colored space is copper).

Test Board Fabrication Files

This is a ZIP file containing the fabrication files used to make the test board prototype.

Test Board BOM

This spreadsheet contains a list of the components in the test board PCB design.

Test Board DNI List

This spreadsheet contains a list of the components from the BOM that were not initially installed on the prototype test boards.

Daughter Board Code

This is the uController code used for the daughter board (p/n: EK-TM4C123GXL) for both the verification board and test board operation.

A.13 Instrument Detector Information

AP-TOF Specification Sheet

List of relevant performance specifications for the mini-TOF MCP detector from Photonis.

AP-TOF Datasheet

This is the datasheet for the mini-TOF MCP detector from Photonis.

A.14 Detector Signal Collector Design

Instrument Signal Block Diagram

This is a drawing to demonstrate the signal as it passes through the instrument.

Instrument Signal Timing Diagram

This is a drawing to show the timing of the control and data signals during the instrument measurement cycle.

Pulse Detection Electronics Block Diagram

This is a drawing to show the components and hardware requirements for the pulse detector electronics.

FPGA Program Diagram

This is a drawing of the main components of the FPGA program for the detector system design.

FPGA Program MATLAB Files

This folder contains files for the MATLAB simulation of the FPGA detector system program. It includes Simulink files for the synchronous and asynchronous programs and a variable definition file which can be run to set various parameters of the Simulink simulation.

A.15 Electronics

Electronics Block Diagram

This is a drawing to outline the major electrical components in the instrument design.

A.16 Project References

Literature Review

This folder contains any available PDFs of sources used for the literature review.

BNG Fabrication

This folder contains a PDF of the published BNG fabrication technique used by SDL to create miniature BNGs.

SDL BNG Artifacts

This folder contains drawings, pictures, and measurements related to the miniature BNG built by SDL.